Study of neutral pions in Pb-Pb collisions at $\sqrt{s_{\mathrm{NN}}} = 2.76$ TeV with the PHOS detector at ALICE

Graduate School of Science, Hiroshima University
Department of Physical Science

Experimental Quark Physics Laboratory

M134056 Daiki Sekihata

10th.February.2015

Supervisor : Prof. Toru Sugitate

Chief examiner : Prof. Kenta Shigaki
Second examiner : Prof. Masanori Okawa

Abstract

A state of deconfined quarks and gluons, called quark-gluon plasma (QGP), is created in high-energy heavy-ion collisions. The ALICE experiment is one of the heavy-ion collider experiments at the LHC to investigate such the new state of matter. Neutral mesons such as π^0 that decays into two photons are suitable to study parton energy-loss in the QGP, since they can be identified by a fine-segmented electromagnetic calorimeter in a wide p_{T} range. It is quite competitive with respect to other particle identification methods. The energy-loss results in a suppression of hadrons yields quantified with a nuclear modification factor R_{AA} defined as hadron yields in A-A collisions with respect to those in p-p collisions. Partons created by a hard scattering interacts with the medium and lose energy. This phenomenon modifies hadron yields at a high p_{T} and can be powerful probe to disentangle mechanism of the energy-loss in the QGP. The Photon Spectrometer (PHOS) in the ALICE is an electromagnetic calorimeter located at 4.6 m from the interaction point. It consists of 10,752 segments with a $2.2 \times 2.2 \times 18$ cm^3 $PbWO_4$ crystal read out by an APD operated at -25 °C to increase yields of scintillation lights. This fine granularity and high-energy resolution allow us to distinguish two photons decayed in a small opening angle from a parent particle at a high p_{T}. I analyzed the Pb-Pb data at $\sqrt{s_{\mathrm{NN}}}$ = 2.76 TeV taken in 2011 with an integrated luminosity $100\mu\mathrm{b}^{-1}$ and detected with centrality triggers. First, I did quality assessment, called QA analysis, to start physics analyses. For example, checking the average cluster energy and the multiplicity in each PHOS module, are performed then I created maps of noisy or dead channels. I extracted clear π^0 peaks in a p_{T} range from 1 to 35 GeV/c and each centrality class via di-photon channel with the PHOS. Finally, R_{AA} is calculated based on yields in Pb-Pb collisions and Tsallis fitting to those in p-p collisions[1]. I will report results of my analyses, namely invariant yields of π^0 and R_{AA}. The nuclear modification factor R_{AA} of π^0 reaches at 0.12 in the most central Pb-Pb collisions.

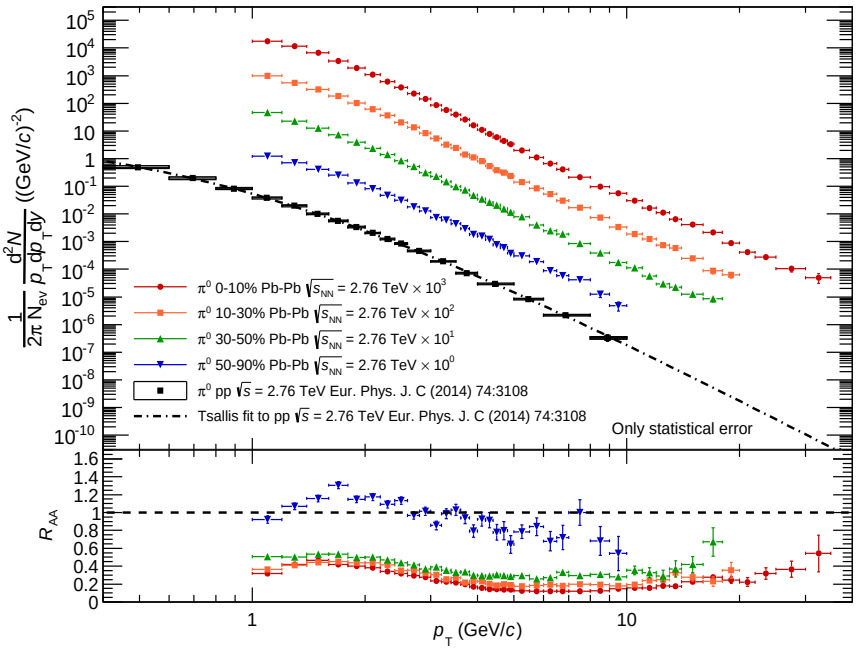

Figure 1: Invariant yield and R_{AA} of π^0 in Pb-Pb collisions at $\sqrt{s_{\mathrm{NN}}} = 2.76$ TeV with the PHOS detector

Contents

List of Figures

List of Tables

1 Introduction

The basic knowledge and background of this experiment and physics are described in this section.

1.1 Standard model

The theory to describe interactions among elementary particles is the standard model. According to the standard model, there are four kinds of interactions, strong interaction, weak interaction, electromagnetic interaction, and gravitational interaction and particles to carry them, called gauge boson, in our universe. Elementary particles and gauge bosons are summarized on Table 1.

name	1st	2nd	3rd	charge	spin
quark	u (up)	c (charm)	t (top)	$+\frac{2}{3}$	$\frac{1}{2}$
	d (down)	s (strange)	b (bottom, beauty)	$-\frac{1}{3}$	
lepton	e	μ	τ	-1	$\frac{1}{2}$
	ν_e	ν_μ	ν_τ	0	

(a) Elementary particles of Standard model.

force	strong	weak	electromagnetic
range (cm)	10^{-13}	10^{-16}	∞
gauge boson	g	$W^{\pm}, Z$	γ
theory	QCD	GSW	

(b) Gauge bosons

Table 1: Elementary particles and gauge bosons of interactions

1.1.1 Quantum Chromodynamics

QCD is the theory to describe strong interaction between quarks and gluons with color charge (red, blue, green). This QCD predicts a transition to new state of matter called "quark-gluon plasma" where quarks and gluons are deconfined from hadrons at a extremely high temperature and a high energy density. The running coupling constant α_s decreases with momentum transfer Q, as expressed by Eq.1.

$$\alpha_s(Q^2) \propto \frac{1}{\ln(\frac{Q^2}{\Lambda^2_{\mathrm{QCD}}})} \tag{1}$$

where Λ_{QCD} is called QCD scale and about 0.2 GeV. This is a guideline to evaluate whether perturbative method is available or not. If momentum transfer Q is greater than Λ_{QCD} enough, the perturbative method can be used for QCD calculation and in this case, it is sometimes called pQCD. However, in the quark-gluon plasma where plenty of quarks and gluons are present the perturbative method is not applicable.

1.2 Ultra-relativistic heavy-ion collisions

Ultra-relativistic heavy-ion collision is a unique method to create the QGP in our technology now. A nucleus is the most densest of all matters. Colliding this nucleus at high-energy, we can produce high energy and high density matter artificially.

1.2.1 Quark-gluon plasma

Quark-gluon plasma, QGP is deconfined state of quarks and gluons at a high temperature and a high energy density. In hadronic state, quarks, anti-quarks and gluons are confined in a hadron. However, we can create this deconfined state by high-energy heavy-ion collisions. According a calculation based on lattice QCD [2], when the temperature T reaches at $T_c = 10^{12}K$ and energy density ϵ reaches at 1 GeV/fm^3, entropy is expected to get larger as shown on Figure.2. Quarks have colors as an internal degree of freedom. Gluons have same characters. Therefore, when hadron gas transforms to QGP, degree of freedom increase rapidly. The QGP is expected to have existed in a quite short time ($\sim 10^{-6}$ s) after a big bang. A schematic view of a phase diagram of QCD that accelerators can reach is shown on Figure.3.

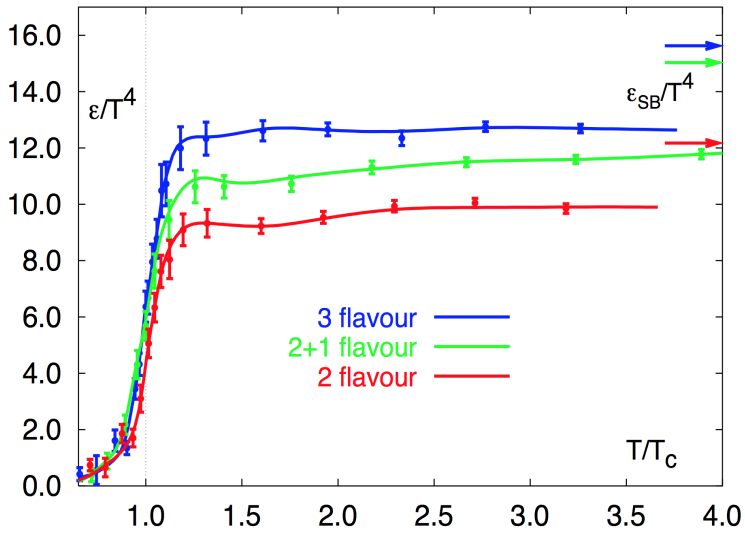

Figure 2: The calculation based on lattice QCD [2]. The degree of freedom of quarks appears at $T = T_c \sim 10^{12}K$.

1.2.2 Schematic view of collision

a. before a collision

A heavy-ion is accelerated up to almost speed of light at high energy. Due to Lorentz contraction, shape of the nucleus becomes flat and radius of the nucleus is multiplied by $\frac{1}{\gamma}$ to the beam direction.

b. parton scattering at initial state

At initial stage of the collision, a structure of nucleons (protons and neutrons) disappears. Quarks and gluons deconfined from these nucleons scatter many times.

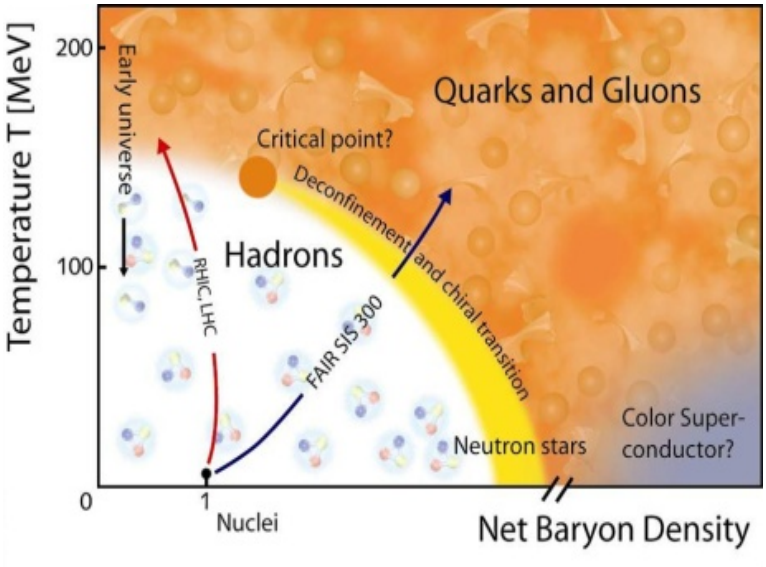

Figure 3: QCD phase diagram.[3]

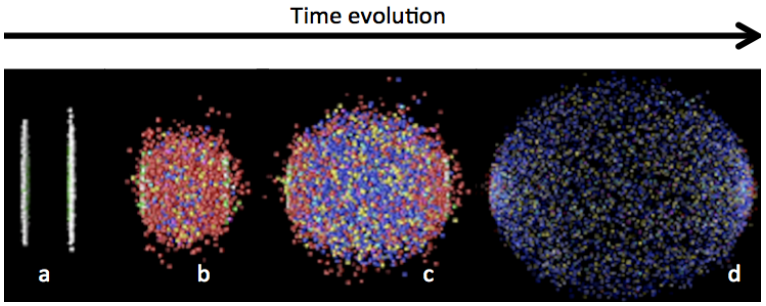

Figure 4: Schematic view of a collision[4].

Heavy quarks such as beauty and charm quark is produced via this initial scattering of partons with high energy. Jets are also produced through this process.

c. QGP phase and thermalization
Reaction zone leaves a trail behind the spectator. Many partons are produced in this region. A "fire ball" which reaches thermal equilibrium at high temperature is created and this is called "quark-gluon plasma". After this phase, this hot and dense matter expand due to high pressure from inside of it.

d. hadronization
The temperature of this matter gets cold because of the rapid expansion. Partons re-combines with each other, and an intermediate state between deconfined stage and hadron gas is created. Finally, the state of matter becomes hadron gas.

We can measure hadrons, leptons and photons only after all processes.

1.2.3 Glauber model calculation

The Glauber model is used to describe the dependence of the number of participant $N_{\rm part}$ and the number of binary collision $N_{\rm coll}$ on impact parameter b in p-A and A-A collisions. Geometrical values are estimated by simulating a lot of nucleons-nucleons collisions based on the nuclear density function described by Eq.2 [5]. These values are calculated to determine centrality of each collision.

$$\rho(r) = \rho_0 \frac{1+w(r/R)^2}{1+\exp(\frac{r-R}{a})} \tag{2}$$

$$\begin{aligned} R &= 6.62 \pm 0.06 \text{ fm} \\ a &= 0.546 \pm 0.010 \text{ fm} \end{aligned}$$

where ρ_0 is the nuclear density for normalization, R is radius of ^{208}Pb, a is the skin thickness of the nucleus and w is a parameter to describe nuclei whose maximum density reaches at radii $r > 0$, $w = 0$ for Pb. Next, simulating a nuclear collision is performed. The impact parameter b is selected randomly from $0 < b < 20$ fm. The nucleus-nucleus collision is simulated as sequential and independent binary nucleon-nucleon collision. Each nucleon is assumed to go straight. Two nucleons from different nuclei are assumed to collide if the transverse distance between center of nuclei is less than $\sqrt{\sigma^{\rm inel}_{\rm NN}/\pi}$[5]. Finally, the number of binary collisions $N_{\rm coll}$ and the number of participants $N_{\rm part}$ are determined by counting respectively.

1.3 Hadron measurement in HIC

Why the measurement of hadrons, especially neutral mesons is important and its advantages are described in this section.

1.3.1 Suppression of hadrons at high $p_{\rm T}$

One of the results to indicate the QGP is suppression of hadrons at high $p_{\rm T}$ region in Pb-Pb collisions. The suppression of hadron yields is defined as Eq.3.

$$R_{\rm AA} = \frac{{\rm d}^2N/{\rm d}p_{\rm T}{\rm d}y\big|_{\rm AA}}{T_{\rm AA} \times {\rm d}^2\sigma/{\rm d}p_{\rm T}{\rm d}y\big|_{\rm pp}} = \frac{{\rm d}^2N/{\rm d}p_{\rm T}{\rm d}y\big|_{\rm AA}}{N_{\rm coll} \times {\rm d}^2N/{\rm d}p_{\rm T}{\rm d}y\big|_{\rm pp}} \tag{3}$$

This parameter is called the nuclear modification factor, and means the ratio of yields in A-A collisions with respect to those in pp collisions. The strong suppression is observed in the most central collision and get weak toward peripheral collisions. This mechanism can be explained by following:
Hadrons with high $p_{\rm T}$ are produced by hard-scatterings of partons at initial stage of collisions. Such hadrons lose their original energies through traversing a strongly interacting matter in A-A collisions. Thus, the nuclear modification factor exhibits one of the properties in the QGP. Figure.5 shows $R_{\rm AA}$ of various hadrons. Direct photons are not suppressed, but, π^0, η containing u, d quarks and K, ϕ containing a s quark are suppressed at the same level respectively. This results in indication of energy-loss at quark level in the QGP. There are two processes to lose parton's energy in the QGP. One is the collisional process, and the other is radiation of gluons in the color field.

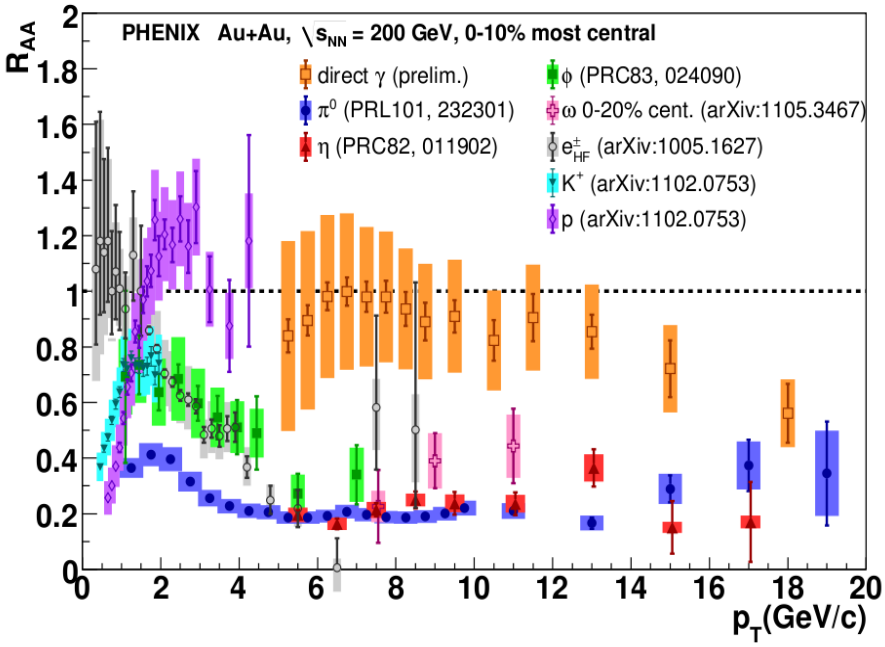

Figure 5: The summary of R_{AA} in PHENIX[7].

1.4 Photon measurement in HIC

Since photons are not involved in the strongly interacting matter, they can provide us information at initial state of the QGP. However, photons are produced at every stage of the collision. So, we can measure only inclusive photons and separate them only statistically. These photons are classified by their origin.

1.4.1 Decay photon

Photons from hadrons are called "decay photon". A list of hadrons that can decay into photons is summarized on Table.2. These hadrons are strong probes to study energy-loss in the QGP by calculating R_{AA}, as described in section1.3. On the other hand, they are huge background to measure direct photons.

Table 2: list of neutral mesons that decay into photons

meson	π^0	η	ω	K_s^0
mass (MeV/c^2)	135	548	783	498
decay mode	2γ	2γ	$\pi^0\gamma(\rightarrow 3\gamma)$	$2\pi^0(\rightarrow 4\gamma)$
branching ratio (%)	98.8	39.3	8.28	30.7
fraction in decay photon (%)	85	10	a few	a few

1.4.2 Direct photon

Direct photons are defined as photons other than decay photons in inclusive photons by Eq.4. They are from Compton scattering between a quark and a gluon ($q(\bar{q})+g \rightarrow q(\bar{q})+\gamma$) and an annihilation of quarks ($q + \bar{q} \rightarrow g + \gamma$). Direct photons can be extracted by subtracting decay photons from inclusive photons statistically. Yields of $\pi^0 \rightarrow \gamma\gamma$ is the largest source in hadron decay photon. From this point of view, π^0 measurement is an important part in heavy-ion collisions.

$$\begin{aligned} \gamma^{\mathrm{direct}} &= \gamma^{\mathrm{inclusive}} - \gamma^{\mathrm{decay}} \\ &= \gamma^{\mathrm{inclusive}} \times \left(1 - \frac{1}{R_\gamma}\right) \end{aligned} \tag{4}$$

$$R_\gamma = \frac{\gamma^{\mathrm{inclusive}}}{\gamma^{\mathrm{decay}}} = \frac{\gamma^{\mathrm{inclusive}}_{\mathrm{data}}/\pi^0_{\mathrm{data}}}{\gamma^{\mathrm{decay}}_{\mathrm{M.C.}}/\pi^0_{\mathrm{M.C.}}}$$

where R_γ is a double-ratio of measured inclusive photon yields to π^0yields in real data to Monte-Carlo which contains only decay photons. This double-ratio means how much excess there are in real measurement with respect to decay photons. If $R_\gamma > 1$, direct photons exist. Additionally, the direct photon is also divided into two groups[6].

Thermal photon

If the hot and dense matter, namely the thermalized QGP is created in the heavy-ion collision, emission of photons will take place. Excess of direct photons will appear in a few GeV/c region. Direct photon from this thermal emission is especially called "thermal photon".

Prompt photon

In a high p_{T} region, photons from the initial parton scattering, like $\gamma-$jet is dominant in direct photons. Thus, photons at from this initial scattering is called "prompt photon".

1.5 Purpose of my thesis

I have two purposes for this π^0 measurement. One is to study parton energy-loss in the QGP. As described above, π^0 can be identified at high a p_{T} region with a fine-segmented electromagnetic calorimeter. This is a unique way to study the energy-loss with an identified particle, not jet, at high p_{T}. The nuclear modification factor R_{AA} of various hadrons has been measured in the PHENIX. These results indicate the energy-loss associates with mass ordering of quarks. R_{AA} of π^0 at higher p_{T} can constrain models strictly to describe the heavy-ion collision. The other one is to measure direct photons that provide us information at the initial stage of the collision. $\pi^0 \rightarrow \gamma\gamma$ is the largest source of decay photons which makes difficult the measurement of direct photons. Direct photons can be extracted by only subtracting decay photons from inclusive photons statistically. π^0 is excellent input to estimate hadron yields that can decay photons such as η, K^0_s, ω because we have much statistics of it. At high p_{T}, prompt photons can be calculated by perturbative QCD since they can traverse the QGP without strong interaction. Therefore, the comparison of direct photons at high p_{T} region with pQCD can prove validity of the measurement. Then,

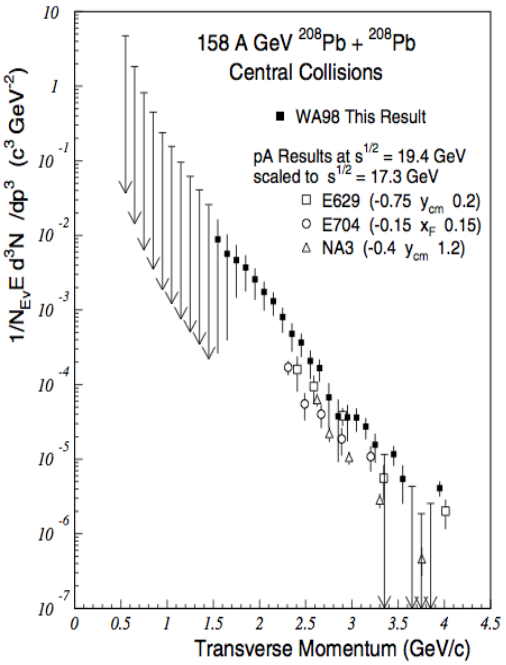

Figure 6: Direct photon yields in WA98[8] at CERN.

we can extract temperature of the thermalized QGP from spectrum of thermal photons at a few GeV/c region. Thus, measurement of π^0 in a wide p_{T} range is powerful prove to disentangle the property of the hot and dense matter.

2 Experimental setup

2.1 Large Hadron Collider (LHC) at CERN

Mainly, four experiments are running at the LHC[9]. They are ALICE (A Large Ion Collider Experiment)[10], ATLAS (A Troidal LHC ApparatuS experiment)[11], CMS (Compact Muon Solenoid)[12] and LHCb [13]. The ATALS and the CMS are multi-purpose experiments at CERN. They focus on searching new particles and discovered Higgs boson in 2012. The LHCb is an experiment to measure new physics in CP violation and rare decay of heavy flavor hadrons. The ALICE is dedicated to study hot and dense matter called QGP (quark-gluon plasma) at the LHC.

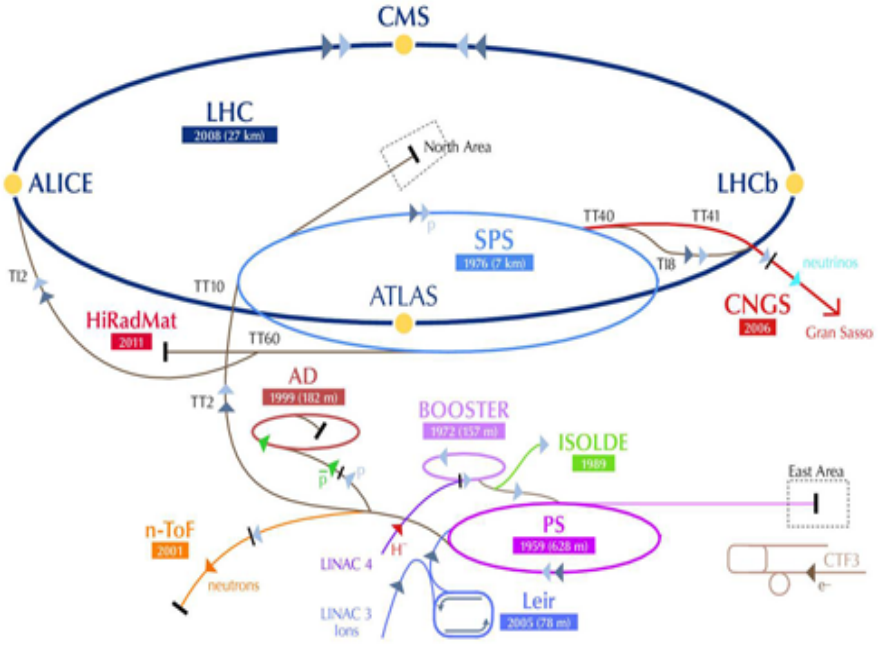

Figure 7: Overview of the accelerator in CERN. [4]

2.1.1 Proton beam production

The source of proton beam is an atom of hydrogen gas. An electron is stripped from the atom in a strong electric field. The proton is accelerated up to 50 MeV in the first accelerator. Second, the proton beam goes to Proton Synchrotron Booster, where the beam reaches at 1.4 GeV. Then, the beam is injected to PS (Proton Synchrotron) to increase up to 25 GeV. The beam goes to SPS (Super Proton Synchrotron) which accelerates to 450 GeV. Finally, the proton beam is transferred to the LHC which accelerates to 7 TeV.

2.1.2 Lead beam production

First, lead atoms are produced by heating lead to 500°C. The vaporized lead atom goes the linear accelerator 3 which use radio-frequency cavities, and electrons of an atom is stripped. The lead ion is injected to LEIR (Low Energy Ion Ring) where it is accelerated

to 72 MeV. Then, it goes to PS and proceed same way as the proton beam as described in 2.1.1.

2.2 ALICE Detectors

Characters and Performances of ALICE detectors are described in this section.

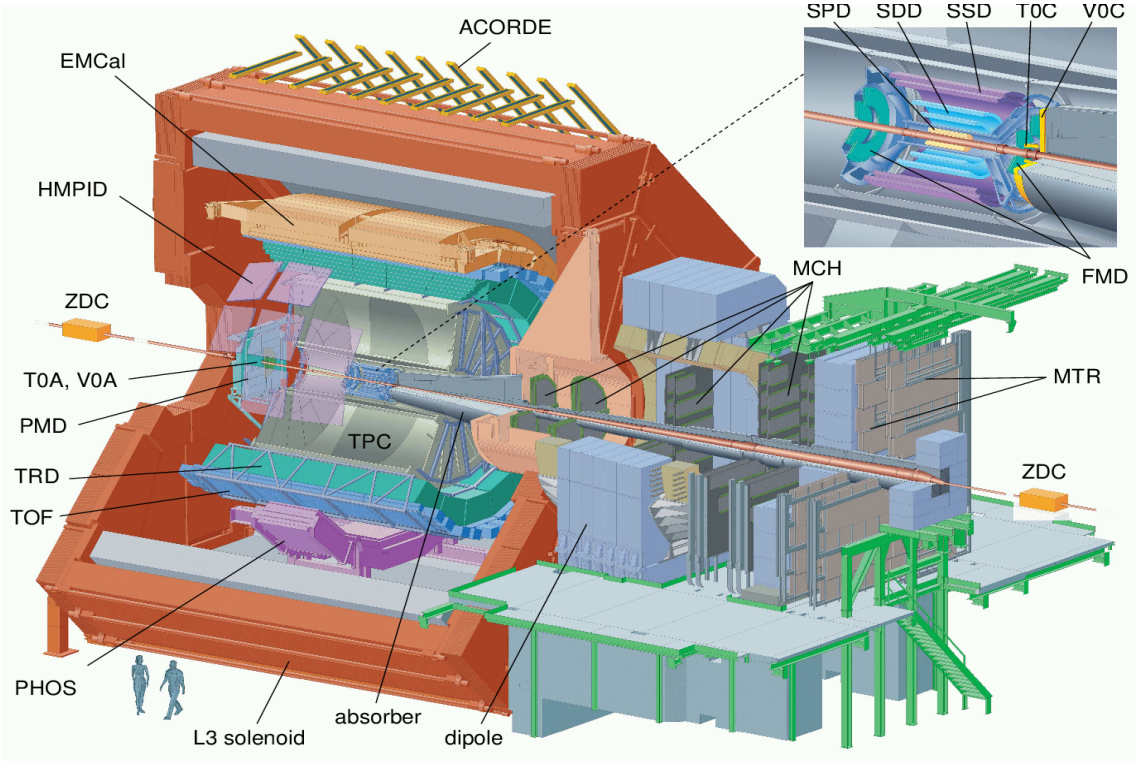

Figure 8: Overview of ALICE detectors. [14]

2.2.1 Central trigger detectors

V0 detector

The V0 detector consists of two arrays of plastic scintillators which locate at A-side(V0A) and C-side(V0C). They cover $2.8 < \eta < 5.1$ (V0A) and $-3.7 < \eta < -1.7$ (V0C) in the pseudo-rapidity. This detector mainly plays two roles in the ALICE. One is providing minimum-bias triggers for pp, p-A and A-A collisions. Another one is to estimate centrality classes in A-A collisions.

T0 detector

The T0 detector measures a collision time precisely. This timing information is used as a start timing for TOF detector and to determine a primary vertex position. Then, this detector provides a L0 trigger when the vertex position is within a preset value to reduce misidentifying beam-gas interactions. This detector also consists of two parts called T0A and T0C. Their coverage are $4.6 < \eta < 4.9$ (T0A) together with FMD, PMD and V0A and $-3.3 < \eta < -3.0$ (T0C) in the pseudo-rapidity.

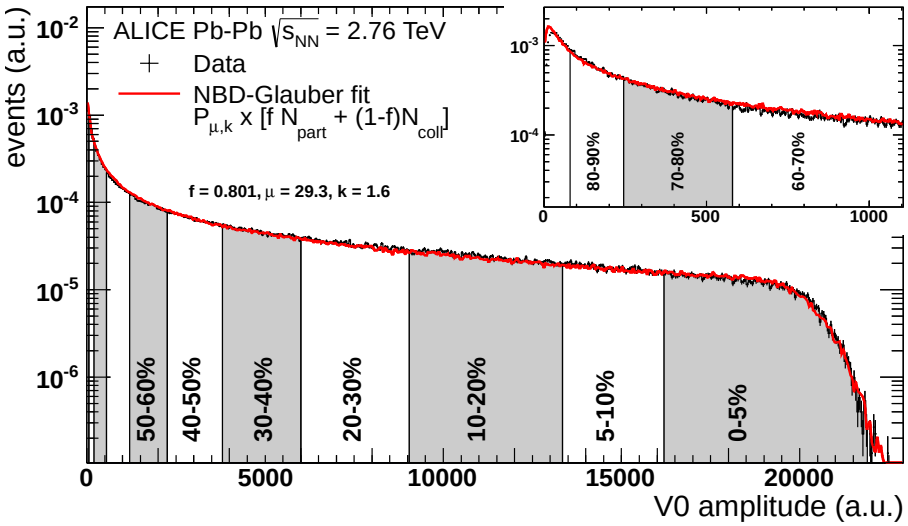

Figure 9: V0 amplitude and centrality determination[14].

2.2.2 Central Tracking System

Inner Tracking System (ITS)

The ITS is a tracking detector which covers the pseudo-rapidity range $|\eta| < 0.9$, composed of three parts of silicon devices. The innermost two layers are Silicon Pixel Detector called SPD because the high particle density is expected in heavy-ion collisions. Then, the middle two layers are Silicon Drift Detector(SDD) and outermost layers are double-sided Silicon Strip Detector (SSD). In addition, this ITS can be used to determinate the primary vertex position and for the stand-alone particle identification via energy-loss $\frac{dE}{dx}$ at low transverse momentum by analogue readout from four outer layers.

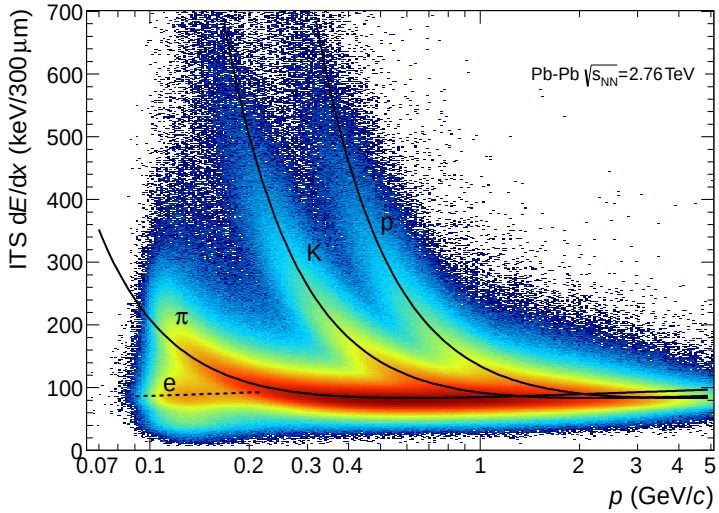

Figure 10: $\frac{dE}{dx}$ distribution in the ITS. [14]

Time-Projection Chamber (TPC)

The TPC is the main tracking detector in the central barrel. This measures momentum and $\frac{dE}{dx}$ of charged particles. The information of tracks is used for charged-particle-veto by non-match with hits on calorimeters that locate at the outside of the TPC. On the other hand, this information is used for particle-identification by matching with tracks measured in ITS, TRD and with hits on TOF, EMCal.

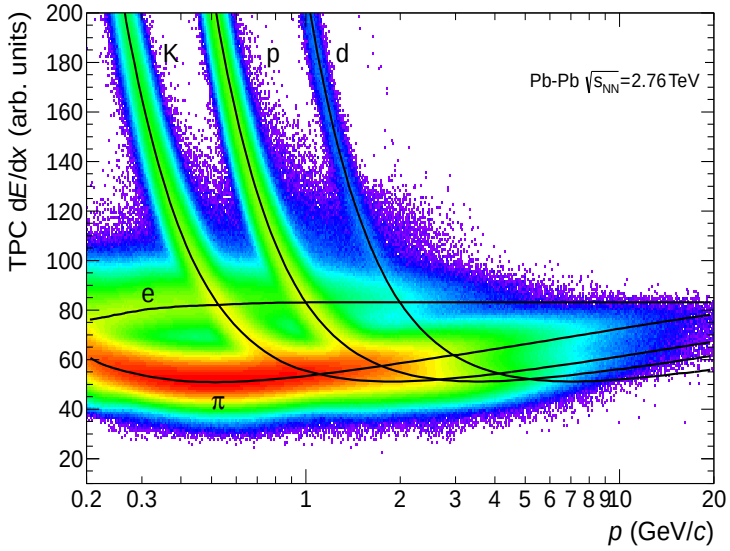

Figure 11: $\frac{dE}{dx}$ distribution in the TPC. [14]

2.2.3 Electromagnetic calorimeter

ElectroMagnetic Calorimeter (EMCal)

The EMCal is installed to explore the physics in jet quenching over the large transverse momentum range accessible in heavy-ion collisions at the LHC. The EMCal is a lead scintillator sampling calorimeter located at a radius about 4.5 m from the interaction point. Its coverage is $|\eta| < 0.7$ and $\Delta\phi = 110°$. The combination of the EMCal and tracking systems with the modest strength of magnetic field 0.5 T in ALICE allows us to reconstruct jets at low transverse momentum region.

PHOton Spectrometer (PHOS)

The PHOS detector is designed for two physics topics mainly. One is to measure single photons at a few GeV region. The other one is to measure neutral pions that can decay into two photons in high transverse momentum range. The PHOS detector consists of 10752 lead-tangstate ($PbWO_4$) crystals readout by APDs. The size of each crystal is $2.2 \times 2.2 \times 18$ cm^3. The $PbWO_4$ crystal has small moliere radius 2.2 cm. Besides, it locates at 4.6 m from the collision point. This fine granularity allows us to distinguish two photons decayed in a small opening angle from π^0 at high p_{T} region.

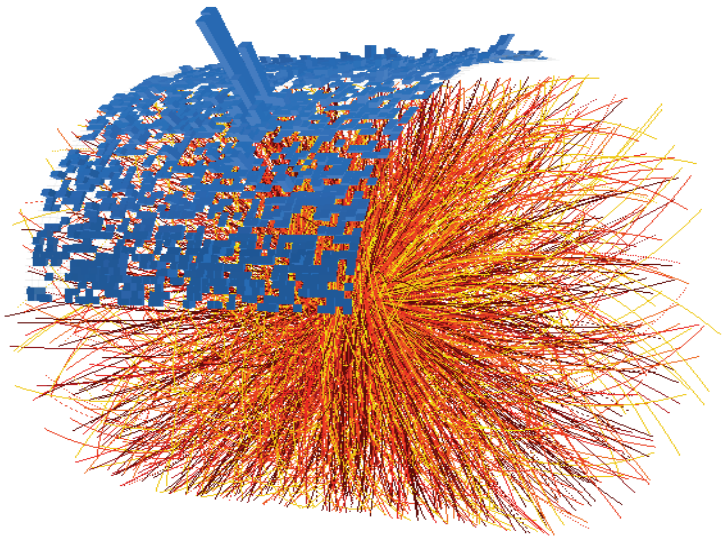

Figure 12: Event display with high p_{T} jet on EMCAL. [14]

2.2.4 PID detectors

Time Of Flight detector (TOF)

The TOF detector is for particle identification in the intermediate momentum range. It is possible to identify π/K below 2.5 GeV/c and $\pi/K/p$ below 4 GeV/c with this detector. In addition, identified kaons allow to study invariant mass of open heavy-flavored states $D^0 \to K^-\pi^+$and low mass vector-meson such as $\phi \to K^+K^-$.

High-Momentum Particle Identification Detector (HMPID)

The HMPID is based on Ring Imaging CHerenkov counter (RICH) and consists of seven modules whose size is 1.5×1.5 m^2 each. The HMPID is installed to identify hadrons at $p_{\mathrm{T}} > 1$ GeV/c, especially π, K, p. This detector enhances capability of PID beyond the momentum range where ITS, TPC via the energy-loss and TOF detector via the time of flight.

Transition Radiation Detector (TRD)

TRD (Transition Radiation Detector) is a detector to identify electrons in the central barrel above 1 GeV/c. Transition radiation (TR) from electrons passing a radiator can be used in combination with $\frac{dE}{dx}$ in suitable mixed gas to reject charged pions above 1 GeV/c in TRD. TPC can provide electron identification via $\frac{dE}{dx}$ below this momentum. It is possible to study the production of vector-mesons and and the quarkonia decayed into the di-electron with combined the data from the ITS, TPC and the TRD in pp collisions as well as Pb-Pb collisions. In addition, it is available to reconstruct open charm and open beauty in semi-leptonic decay with excellent vertex position resolution in the ITS.

2.2.5 Forward detectors

Muon spectrometer

The ALICE can perform muon measurement in the pseudo-rapidity region $-4.0 <$

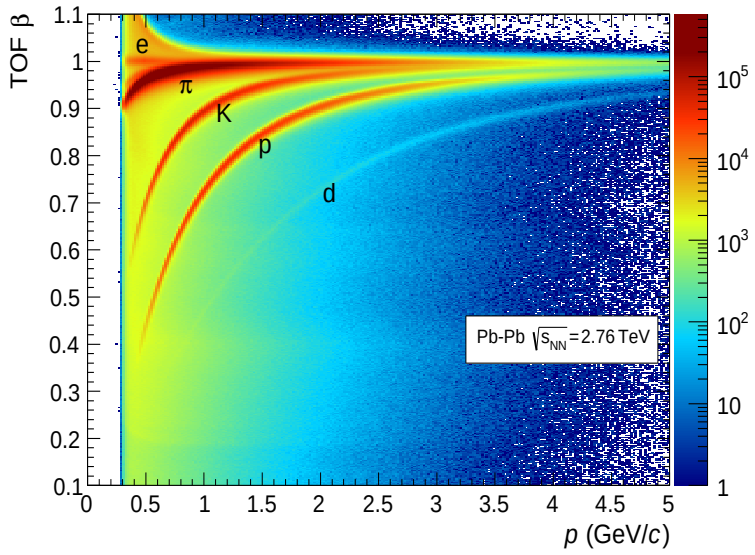

Figure 13: TOF distribution as a function of track momentum. [14]

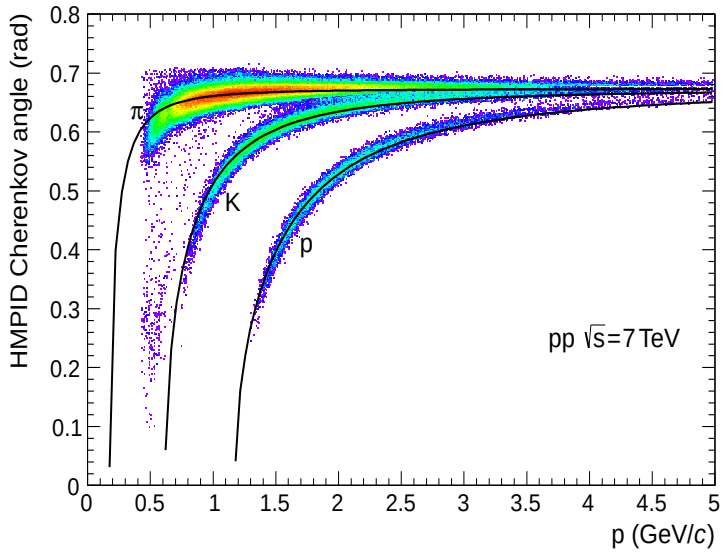

Figure 14: Mean cherenkov angle distribution measured by HMPID in pp collisions at $\sqrt{s} = 7$ TeV as a function of track momentum. [14]

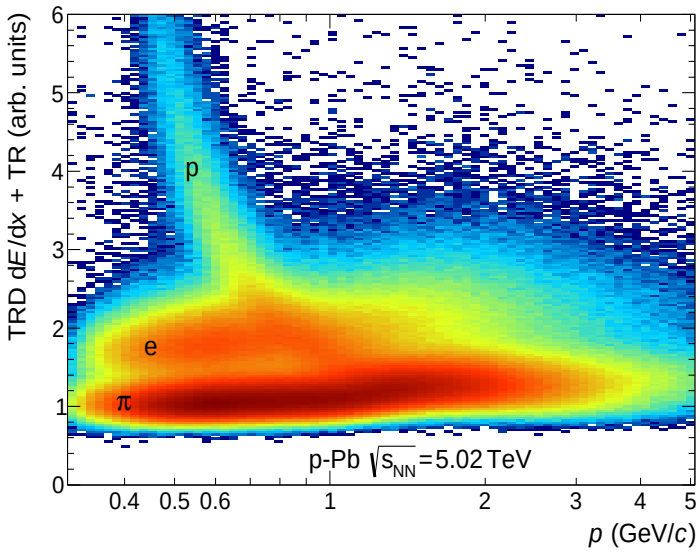

Figure 15: $\frac{dE}{dx}$ distribution in the TRD. [14]

$|\eta| < -2.5$ with this muon spectrometer. The spectrum of vector-meson resonances consisted of heavy-quarks such as J/ψ, $\psi(1s)$, $\psi(2s)$, Υ, $\Upsilon(1s)$ and $\Upsilon(2s)$ will be measured in the di-muon decay channel at forward region. The simultaneous measurement of all kinds of quarkonia with the same detector will allow a direct comparison of their production rate as a function of transverse momentum and centrality.

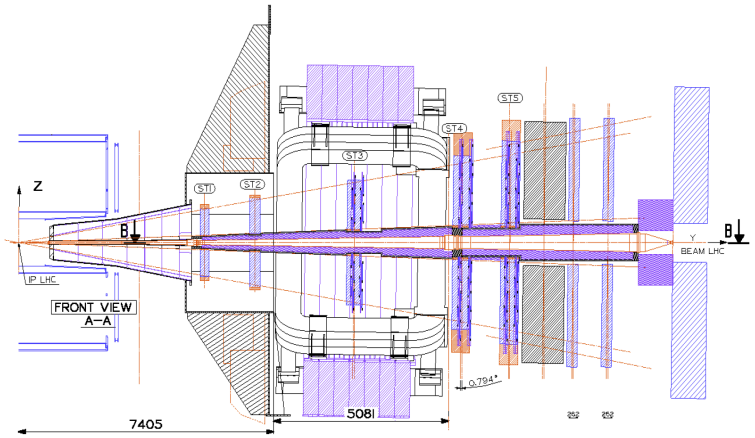

Figure 16: Detector layout of the muon spectrometer. [10]

Zero Degree Calorimeter (ZDC)

The number of participant nucleons is observable directly and is related to the geometry of A-A collisions. It can be estimated by measuring the energy of non-interacting nucleons, called spectator at forward region. Spectator nucleons are detected by this ZDC in ALICE. If all the spectators are detected in this ZDC, the number of par-

ticipants is given by,

$$\begin{aligned} E_{\mathrm{ZDC}}\ (\mathrm{TeV}) &= E_{\text{proton beam}}\ (\mathrm{TeV}) \times \frac{Z}{A} \times N_{\mathrm{spectator}} \\ N_{\mathrm{participant}} &= A - N_{\mathrm{spectator}} \end{aligned}$$

where Z is the number of protons in the Pb nuclei (82), A is a mass number of it (208). The ZDC is able to provide the reaction plane on Pb-Pb collisions. Additionally, The information of centrality from the ZDC is used for centrality trigger in Pb-Pb collisions.

Forward Multiplicity Detector (FMD)
The main purpose of the FMD is to measure charged particle multiplicity in the pseudo-rapidity range $-3.4 < |\eta| < -1.7$ and $1.7 < |\eta| < 5.0$. This information is used for the study of multiplicity fluctuations and reaction plane determination for flow analysis on an event-by-event basis.

Photon Multiplicity Detector (PMD)
The PMD measures multiplicity and spatial distribution of photons in the forward region of $2.3 < |\eta| < 3.7$. These measurements can give estimation of transverse electromagnetic energy E_T and reaction plane on an event-by-event basis. The important information about limiting fragmentation, order of phase transition, the equation of state of matter and formation of disoriented chiral condensates can be extracted from the photon multiplicity.

2.3 The PHOS detector

Many detectors are described in 2.2. More details about the PHOS detector are described in this section.

2.3.1 Detector design

The PHOS detector is a fine-segmented electromagnetic calorimeter installed in the ALICE at the LHC. The PHOS measures energy and hit position of photons and electrons, positrons precisely. Five modules were designed for the ALICE, but, three modules were installed in Run-1. It locates at 4.6 m from the interaction point and the coverage is $260^\circ < \phi < 320^\circ$ in azimuthal angle, $|\eta| < 0.12$ in pseudo-rapidity range. There are 3584 channels consisting of a $2.2 \times 2.2 \times 18$ cm^3 $PbWO_4$ crystal readout by an APD, operated at -25°C to increase light yields on one module. The Moliere radius is 2.2 cm and the radiation length is 0.89 cm in this $PbWO_4$ crystal. On the electronics side, there are two amplifiers, "high gain" and "low gain" channel. The low gain channel starts to operate over the energy 4-5 GeV. Due to two kinds of gains channels, we can measure the energy up to 80 GeV. The small Moliere radius allows us to measure two photons decayed from π^0 in a small opening angle at high p_{T}.

2.3.2 Principle of measurement

The PHOS exploits an electromagnetic shower to measure energy of electrons, positrons and photons. When a photon goes to the PHOS crystal, an electron-positron pair is created by interacting in electric field of nuclei. Then, this electron-positron pair emits

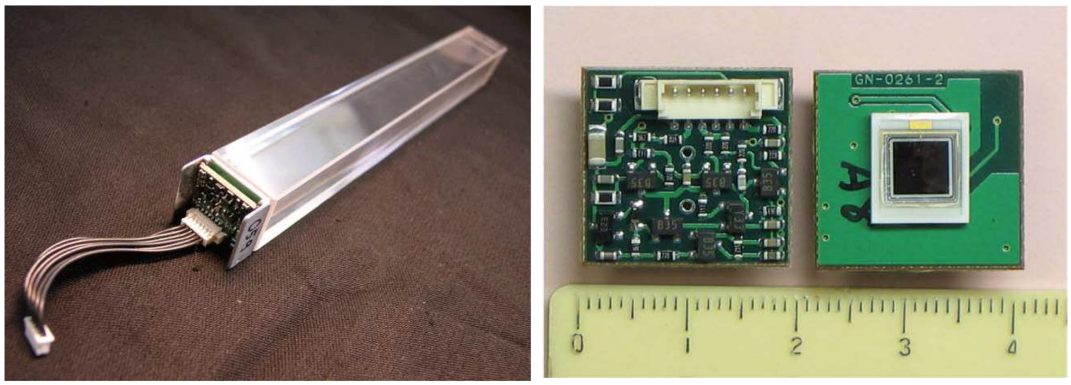

(a) $PbWO_4$ crystal attached with an APD. (b) APD as a photon sensor.

Figure 17: $PbWO_4$ crystal and APD.[10]

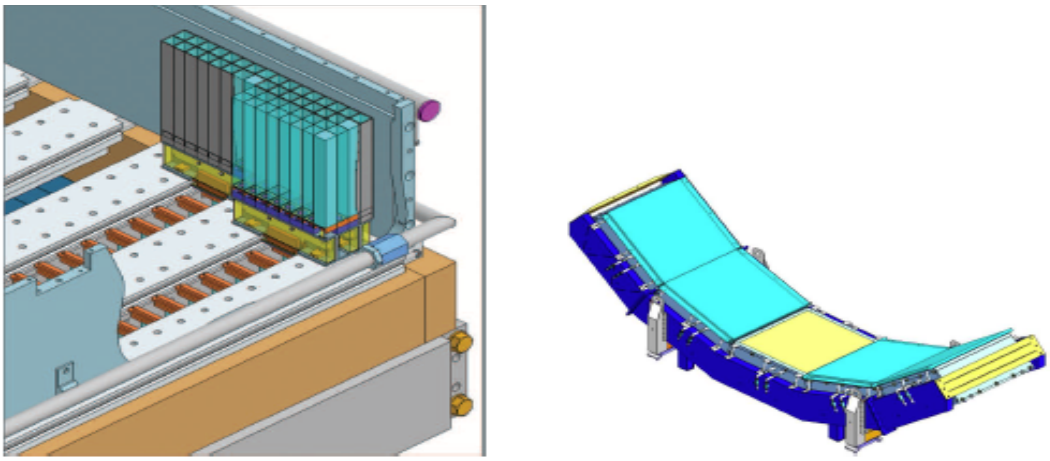

Figure 18: Crystal mapping and PHOS modules.[10]

photons by the bremsstrahlung. Secondary photons will produce electron-positron pair again. These process will repeat until the energy of photon is less than 1 MeV/c^2 (2×0.511MeV/c^2). These electrons and positrons excites electrons in atomic orbit. Excited electrons return to originally stable orbit with emitting extra energy as photon whose wave length $\lambda \sim 400$nm, called "scintillating light". Finally, APD can detect this visible light by an efficiency $\sim$ 80-90%. As the yield of scintillating light is proportional to the energy of incident particle, we can measure the energy of incident particle. On the other hand, in case that charged particle like $\pi^{\pm}$ is incident to $PbWO_4$ crystals, since the probability of bremsstrahlung is small, the shower will not be produced and light yield is very small.

2.3.3 Energy resolution

The energy resolution of an electromagnetic calorimeter is given by Eq.5[16].

$$\frac{\sigma_E}{E\ [\mathrm{GeV}]} = \sqrt{\left(\frac{\mathrm{a}}{E\ [\mathrm{GeV}]}\right)^2 + \left(\frac{\mathrm{b}}{\sqrt{E\ [\mathrm{GeV}]}}\right)^2 + \mathrm{c}^2} \tag{5}$$

where, parameters are following [16]:

$$\begin{aligned} a &= 0.0130 \pm 0.0007 \text{ GeV} \\ b &= 0.036 \pm 0.002 \sqrt{\text{GeV}} \\ c &= 1.12 \pm 0.3 \text{ \%} \end{aligned}$$

2.3.4 Spatial resolution

The spatial resolution of the PHOS detector is given by Eq.6 [17].

$$\sigma_{\text{x,y}}[\text{mm}] = \sqrt{\left(\frac{3.26}{\sqrt{E\ [\text{GeV}]}}\right)^2 + 0.44^2} \tag{6}$$

The high spatial resolution is achieved by fine-segmented $PbWO_4$ crystals whose Moliere radius is very small.

2.3.5 Readout system

Front-End Electronics card

This is a main part to readout signals from APDs. One FEE card has one FPGA (Field Programmable Gate Array) which plays a role as a brain and four ALTRO chips to control APD settings. One FEE card can control 32 channels.

Readout Control Unit

RCU is a serial readout system. 14 FEE cards are connected to one RCU. This serial system will be replace with SRU (Scalable Readout Unit) which allows us to readout in parallel.

FAST-OR

FAST-OR signal is analogue sum of 2×2 APD signals generated on each FEE card and sent to the TRU.

Trigger Region Unit

TRU receives FAST-OR signals from 14 FEE cards. L0, L1 trigger is produced on the TRU and sent to the ALICE central readout system.

Table 3: Summary of Components in readout system.

1 FEE	1TRU	1 RCU branch	1 PHOS module
32 APDs 8 analogue outputs	112 analogue inputs	14 FEEs 448 APDs 1 TRU	112 FEEs 8 RCUs 8 TRUs 3584 APDs

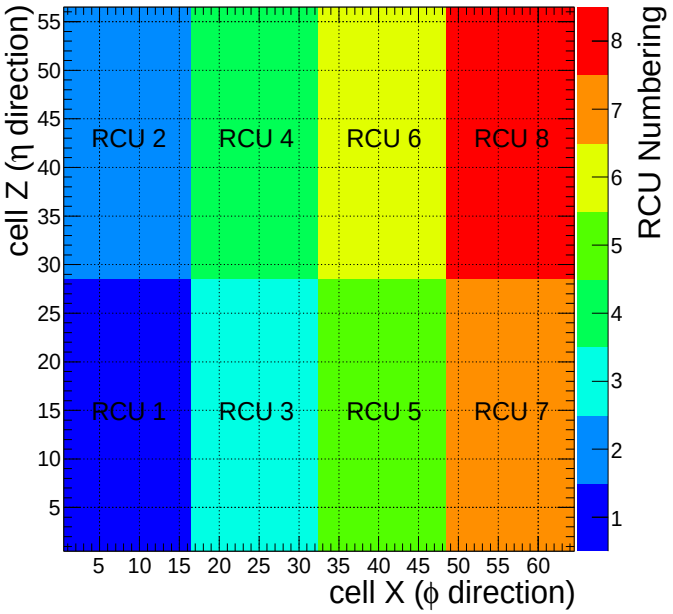

Figure 19: RCU mapping of the PHOS.

2.3.6 Trigger system

The PHOS detector provide L0-trigger signal to CTP (Central Trigger Processor) in the central system. The output signal from APDs are summed by 2×2 on Fast-OR and the sum is sent to the TRU (Trigger Region Unit). The L0 signal is generated at TRU when a sum of 2×2 cell amplitude is higher than a certain threshold. One TRU is installed in each RCU.

3 Analysis

First, Data set and how to qualify these data are shown in this section. Then, how to reconstruct π^0 in real data and to calculate several efficiencies in Monte Carlo are also described.

3.1 Analysis framework in ALICE

The ALICE members have developed our own analysis framework called "aliroot". This is based on "root" developed in CERN and written in C++. The aliroot allows us to reconstruct raw data, simulate and describe ALICE detectors. In addition, the ALICE records much data (∼Peta Byte/year) of collisions. This requires much computing power and storages to handle all data. Thus, these data are separated and locate at different places in the world. This GRID system allows us to access and analyze data easily. A part of machines, called "Tier-2" to calculate our jobs is locating at Hiroshima University and working properly.

3.2 Data set

I analyzed Pb-Pb data taken in 2011 triggered with Minimum Bias and centrality triggers. These data are simply combined because contribution for triggers from the PHOS detector is equivalent in each trigger. Summary of data set and triggers used in this analysis taken by ALICE in 2011 are Table 4.

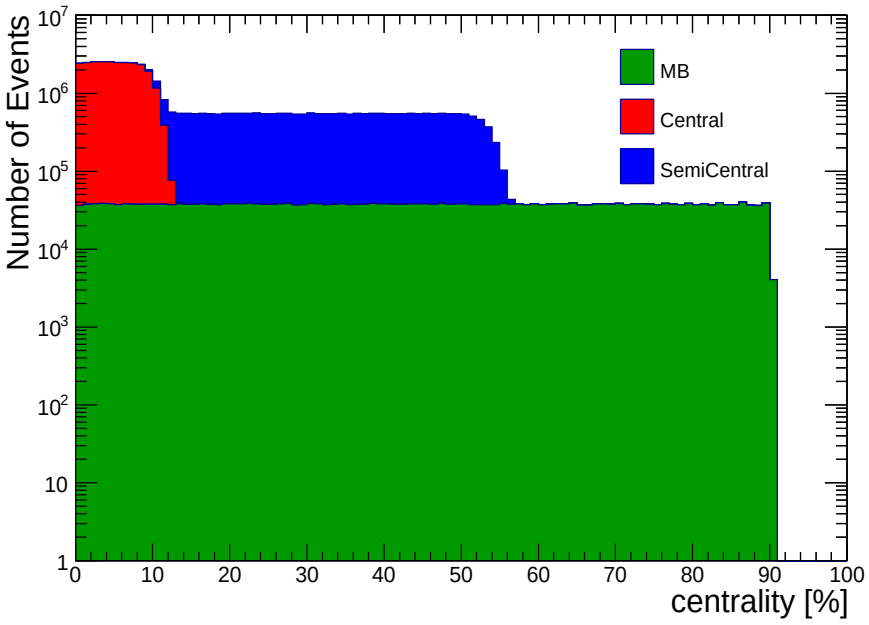

Figure 20: Centrality distribution in my analyses.

Trigger criteria are following:

Minimum Bias
: At least one hit on each V0A and V0C.

Table 4: Data set and triggers used in this analysis.

Trigger	Minimum Bias	Central	Semi-Central
Analyzed N_{events}	2.4 M	20 M	18 M
Centrality range (mainly)	0-90 %	0-10 %	10-50 %

Central trigger
At least one hit on each V0A and V0C
&& primary vertex within ±10cm
&& high multiplicity in V0 detector.

Semi-Central trigger
At least one hit on each V0A and V0C
&& primary vertex within ±10cm
&& low multiplicity in V0 detector.

Pb-Pb data at $\sqrt{s_{NN}} = 2.76$ TeV is also taken in 2010. However, since this was first Pb-Pb run at the LHC, data has been taken in almost Minimum Bias trigger. It recorded about 25 M events in centrality range 0-90 %. Therefore, I analyzed 2011 data to gain about ten times much statistics in most central collisions than that in 2010 data.

3.3 Quality assessment

The data is expected to be recorded information such as energy, momentum and hit position exactly. However, as all detectors including PHOS have effects to smear these informations, conditions of PHOS detector like dead or noisy channels must be understood before starting physics analyses. Thus, quality assessment was performed at a RCU (Readout Control Unit) level and I created normal run list and PHOS bad channel maps for Pb-Pb data in taken 2011.

3.3.1 Run selection

This analysis was performed for run selection. First, all runs that include the PHOS as a readout and a trigger detector are listed up. For this step, there are 150 runs. In these 150 runs, runs with unexpected behavior of PHOS detector, like noisy or dead conditions, need to be removed based on average cluster multiplicity and average cluster energy. They are defined as a following equation respectively.

$$\text{average cluster multiplicity} < N_{cluster} > = \frac{\sum_{event\ i}^{N_{event}} N^{i}_{cluster}}{N_{event}} \tag{7}$$

$$\text{average cluster energy} < E_{cluster} > = \frac{\sum_{event\ i}^{N_{event}} \sum_{cluster\ j}^{N^{i}_{cluster}} E^{j}_{cluster}}{\sum_{event\ i}^{N_{event}} N^{i}_{cluster}} \tag{8}$$

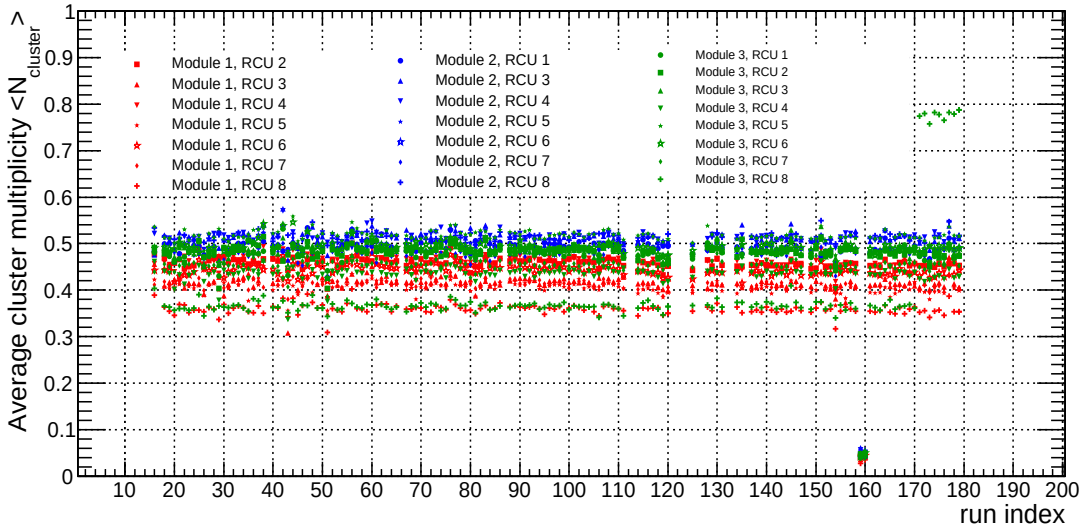

Figure 21: Average cluster multiplicity $N_{cluster}$ in each run.

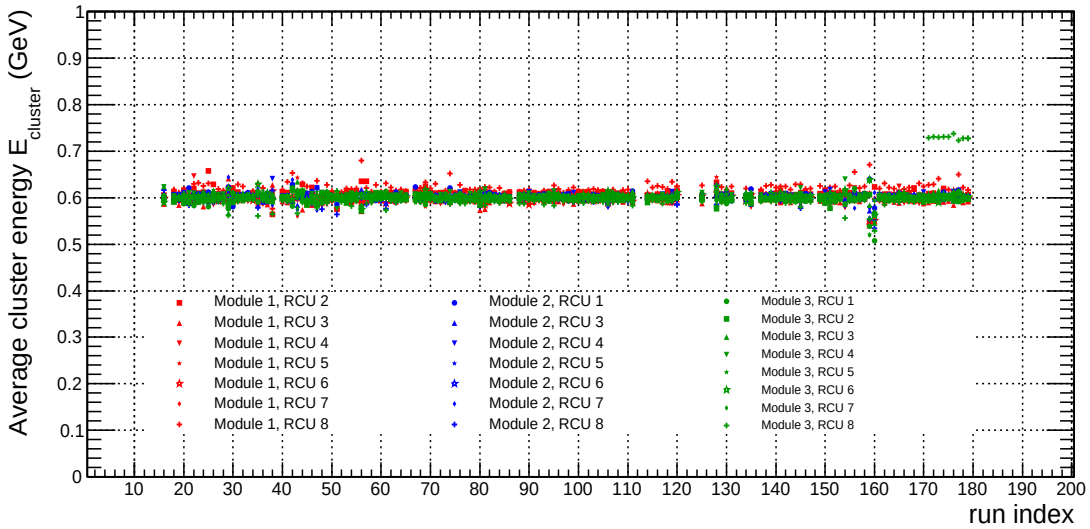

Figure 22: Average cluster energy $E_{cluster}$ in each run.

According to my QA analysis, there are two runs (run index 159 and 160) with too few clusters. They correspond to official run number 170267 and 170168 respectively. The big jump have been found in both average cluster energy and average cluster multiplicity on module3-RCU8 over the run index 170. This is because HV setting for APDs on this branch has been changed. So, I removed these two runs (170267 and 170268) from my physics analyses and decided not to use clusters on module3-RCU8 in all runs.

3.3.2 PHOS bad maps

Then, I created bad channel maps of the PHOS detector in Pb-Pb data taken in 2011. These bad maps are based on the number of fired times of each cell in Minimum Bias data.

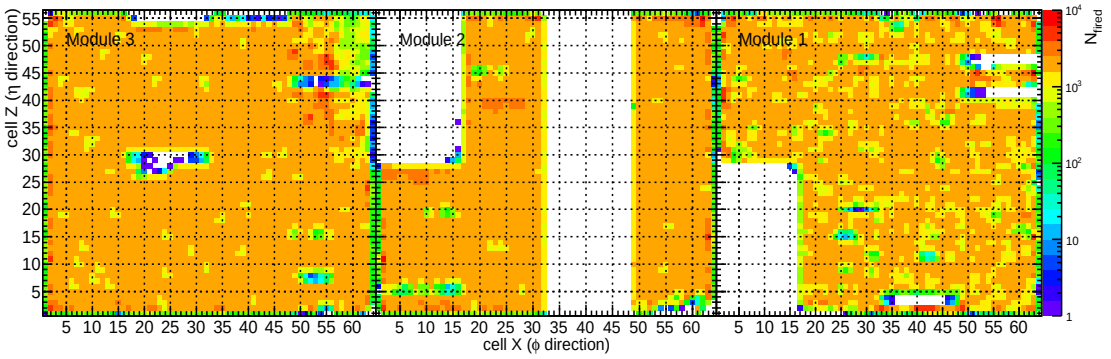

(a) Low energy clusters $0.5 < E_{\mathrm{cluster}} < 2.0$ GeV.

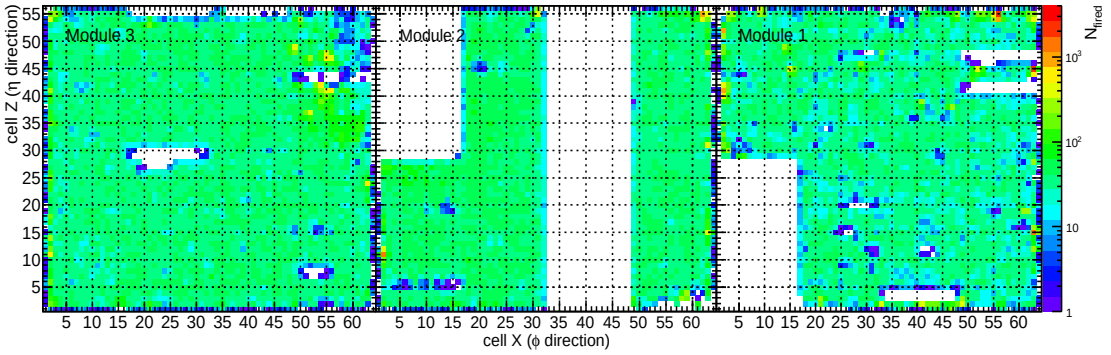

(b) High energy clusters $E_{\mathrm{cluster}} \geq 2.0$ GeV.

Figure 23: Hit map of clusters. Module1-3 from right to left. The color band on the right side shows the number of fired times. Red means noisy channels and purple means channels with few response. Unfortunately, white area shows dead channels.

Figure.23 shows hit maps of clusters. One cluster consists at least 3 cells. So, the center of gravity in the energy of cluster is filled as a cluster position. As a next step to create bad maps, I made a 1-dimension histogram of the number of fired times in each low and high energy clusters from hit maps. Fitting around peak position in each module by Gaussian function, I decided cells in range of peak position $\pm 3\sigma$ in both histograms of low energy and high energy clusters were normal cells. Finally, if the center of gravity in a cluster

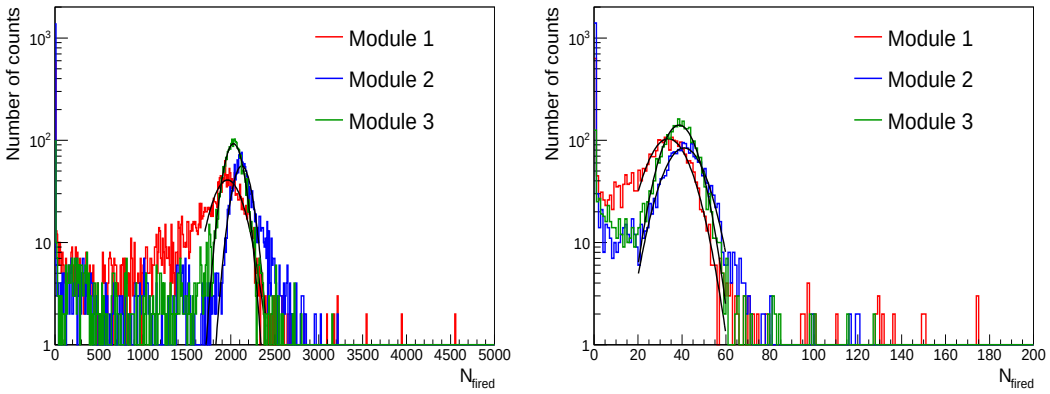

(a) Low energy clusters. (b) High energy clusters.

Figure 24: The distributions of the number of fired times.

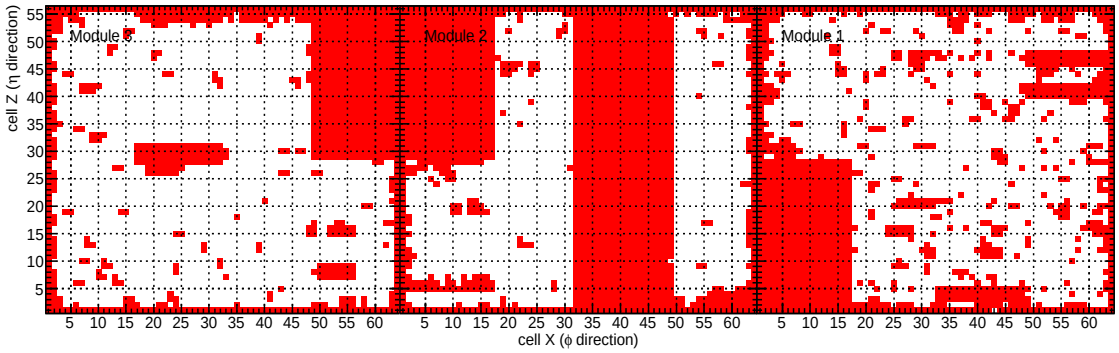

Figure 25: PHOS bad channel maps applied for my analyses. Module1-3 from right to left.

energy locates on a bad cell, this cluster is removed from analyses.

3.4 Analysis cuts

Cut criteria to select photon clusters are described in this section.

3.4.1 Common cluster cut

MIP cut

This cut is for removing Minimum Ionizing Particle. The parameter depends on the materials of the PHOS detector. The energy of MIP E_{MIP} is given by an Eq.9.

$$\begin{aligned} E_{\mathrm{MIP}}\ (\mathrm{MeV}) &= \rho\ (\mathrm{g/cm^3}) \times \left.\frac{dE}{dx}\right|_{\mathrm{MIP}} (\mathrm{MeV \cdot cm^2/g}) \times L\ (\mathrm{cm}) \\ &= 8.28 \times 2 \times 18 \approx 300\ (\mathrm{MeV}) \end{aligned} \tag{9}$$

Where ρ is a density of the $PbWO_4$ crystal, $\left.\frac{dE}{dx}\right|_{\mathrm{MIP}}$ is the energy-loss of the MIP and L is the length of the $PbWO_4$ crystal. Thus, I selected clusters with its energy greater than 0.3 GeV.

N_{cell} cut
: This N_{cell} cut is simply for reject clusters created from the noise of electronics in the PHOS detector. Clusters consisting of at least three cells were selected.

TOF cut
: The TOF cut is to distinguish which collision the cluster comes from. Unfortunately, the PHOS records clusters from other collisions because of a wide time-window to shape up a APD signal. An interval of each Pb-Pb collision is 200 ns in 2011 at the LHC. So, $TOF_{cluster}$ is required within $\pm$100 ns from a start signal.

3.4.2 CPV cut (Charged Particle Veto)

Charged-particle-veto is performed with tracking detectors (ITS and TPC) inner side of the PHOS detector. Tracks of charged particle measured in tracking detectors are vended due to the magnetic field of the L3 magnet. These tracks are extrapolated to the surface of the PHOS. Then, if a cluster is matched with the extrapolated track, this cluster will be removed. The typical distance between a cluster and a track of charged particle has been studied in HIJING simulation. Therefore, clusters with the distance farther than 2σ to tracks were selected, depending on $p_{\mathrm{T}}$of tracks.

3.4.3 Dispersion cut

The dispersion cut is sometimes called "shower shape cut". Interactions between charged particles, excepted electrons and positrons, and materials are mainly inelastic scattering with molecular or elastic scattering with atoms. As electrons and positrons have light mass, the energy-loss due to bremsstrahlung is dominant process. At high energy, a main interaction between photons and materials is pair-creation of an electron and a positron. Electrons and positrons lose their energies due to bremsstrahlung. If the energy of photons from bremsstrahlung is higher than 1 MeV($\approx 2 \times 0.511$MeV), the pair of an electron and a positron will be created again. These processes are repeated until the energy of photon becomes lower than 1 MeV. For this reason, clusters created by photons can be distinguished with those by others on the PHOS detector. A typical shape of photon cluster has been studied by simulations. This shape is characterized by a parameter R defined as Eq.10. These parameterization is derived from 2-dimensional Gaussian fitting to energy deposits in $PbWO_4$ crystals.

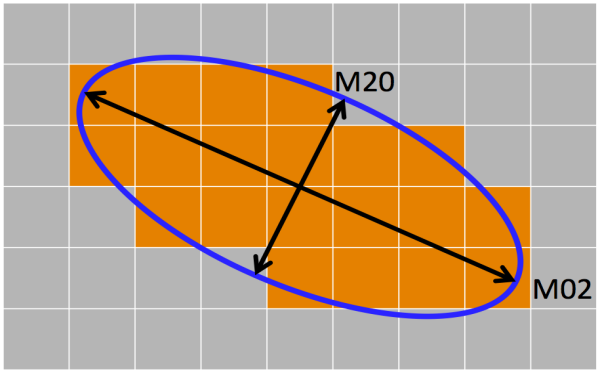

Figure 26: Schematic view of cluster shape created by photon.

$$\begin{aligned} \mathrm{R}^2 &= 0.5 \cdot \frac{(\mathrm{M20} - \langle \mathrm{M20} \rangle)^2}{\sigma^2_{\mathrm{M20}}} \\ &+ 0.5 \cdot \frac{(\mathrm{M02} - \langle \mathrm{M02} \rangle)^2}{\sigma^2_{\mathrm{M02}}} \\ &+ 0.5 \cdot \mathrm{c} \cdot \frac{(\mathrm{M20} - \langle \mathrm{M20} \rangle) \cdot (\mathrm{M02} - \langle \mathrm{M02} \rangle)}{\sigma_{\mathrm{M20}} \cdot \sigma_{\mathrm{M02}}} \end{aligned} \tag{10}$$

$$\begin{aligned} \langle \mathrm{M02} \rangle &= 1.53126 + \frac{9.50835 \cdot 10^6}{1 + 1.08728 \cdot 10^7 \cdot E_{\mathrm{cluster}} + 1.73420 \cdot 10^6 \cdot E^2_{\mathrm{cluster}}} \\ \langle \mathrm{M20} \rangle &= 1.12365 + 0.123770 \cdot \exp(-E_{\mathrm{cluster}} \cdot 0.246551) + 5.30000 \cdot 10^{-3} \cdot E_{\mathrm{cluster}} \\ \sigma_{\mathrm{M02}} &= 6.48260 \cdot 10^{-2} + \frac{7.60261 \cdot 10^{10}}{1. + 1.53012 \cdot 10^{11} * E_{\mathrm{cluster}} + 5.01265 \cdot 10^5 \cdot E^2_{\mathrm{cluster}}} \\ &+ 9.000 \cdot 10^{-3} \cdot E_{\mathrm{cluster}} \\ \sigma_{\mathrm{M20}} &= 4.44719 \cdot 10^{-4} + \frac{6.99839 \cdot 10^{-1}}{1. + 1.22497 \cdot E_{\mathrm{cluster}} + 6.78604 \cdot 10^{-7} \cdot E^2_{\mathrm{cluster}}} \\ &+ 9.000 \cdot 10^{-3} \cdot E_{\mathrm{cluster}} \\ \mathrm{c} &= -0.35 - 0.550 \cdot \exp(-0.391 \cdot E_{\mathrm{cluster}}) \end{aligned}$$

where $\langle \mathrm{M20} \rangle$, $\langle \mathrm{M20} \rangle$ and σ_{M20}, σ_{M02} are average value and standard deviation of M20, M02 in photon cluster respectively. I selected clusters if $\mathrm{R}^2 < 2.5^2$.

3.5 π^0 reconstruction

How to identify π^0 is described in this section.

3.5.1 Invariant mass method

π^0 was identified by its invariant mass which is 135 MeV/c^2, focusing on $\pi^0 \to \gamma\gamma$ decay channel. The invariant mass is calculated with four-momentum of two photons.

$$M_{\gamma\gamma} = \sqrt{(E_1 + E_2)^2 - (\vec{p_1} + \vec{p_2})^2} \tag{11}$$

As the mass of a photon is 0 GeV/c^2, Eq.11 can be simplified.

$$M_{\gamma\gamma} = \sqrt{2E_1E_2 \cdot (1 - \cos\theta_{12})} \tag{12}$$

where θ_{12} is an opening angle between two photons from π^0. This $M_{\gamma\gamma}$ was calculated over all combination in each event. For example, when there are 10 photon clusters in a event, ${}_{10}\mathrm{C}_2 = 45$ combinations are considered. In addition, a parameter α which means asymmetry between energies of decayed two photon, based on kinematics, were introduced to increase π^0signal in this analysis. As the coverage of the PHOS detector is small ($260^\circ < \phi < 320^\circ$ in azimuthal angle, $-0.12 < \eta < 0.12$ in pseudo-rapidity), if this energy asymmetry is large, such combination can not be from π^0.

$$\alpha = \frac{|E_1 - E_2|}{E_1 + E_2} \tag{13}$$

In my analyses, combinations with $\alpha < 0.7$ were selected.

3.5.2 Event mixing technique

The event mixing technique is a technique to subtract combinatorial backgrounds in extracting π^0 yields. We can measure π^0 yields only statistically. As described in 3.5.1, if there are 10 photon clusters (two clusters from $\pi^0 \to \gamma\gamma$ and eight clusters from others) in a event, ${}_{10}\mathrm{C}_2 = 45$ combinations must be considered. Nevertheless, only one combination is from π^0. To subtract this huge combinatorial background, the event mixing technique was introduced. A schema of this is calculate invariant mass between one cluster in certain event and one cluster from other events. In same events, there are both signals and backgrounds, but there are only background in mixed events. A invariant mass spectrum is shown on Figure.27, as a example.

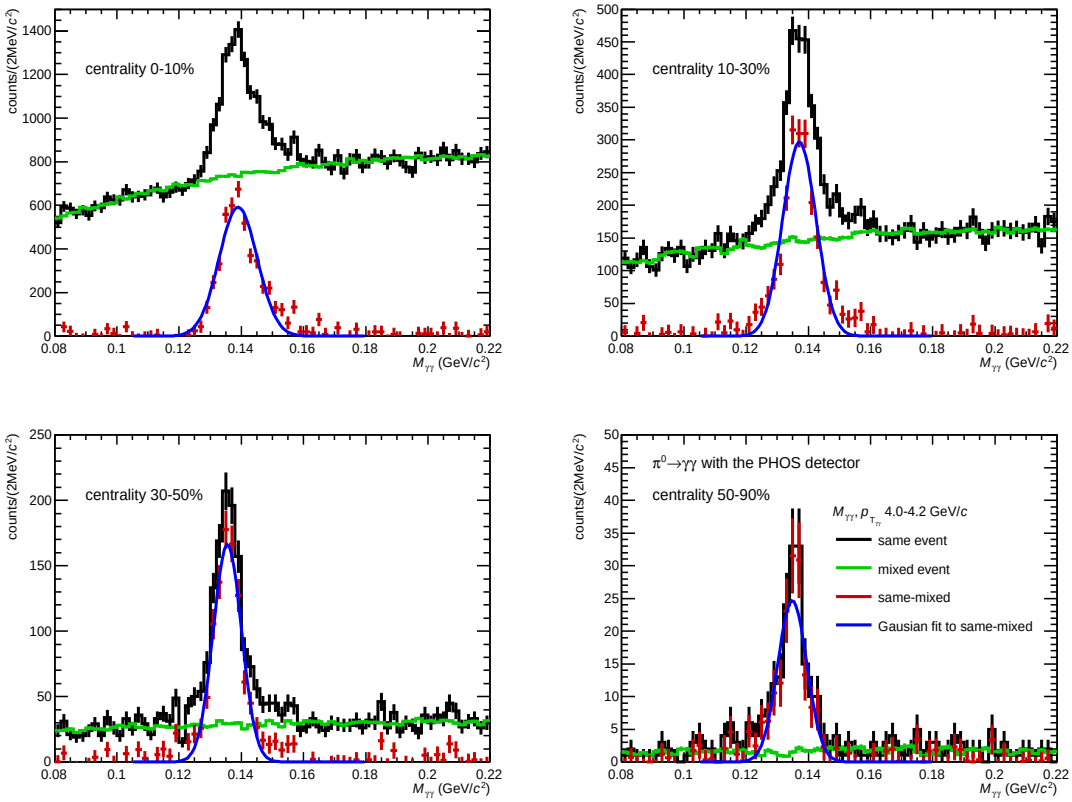

Figure 27: Invariant mass spectra with two photons candidates in the most central Pb-Pb collisions.Black point shows invariant mass spectrum in same event, green shows combinatorial background reproduced by the event mixing technique. A clear π^0 peak is extracted as shown by red.

3.6 Monte Carlo analysis

Monte Carlo simulation was used to calculate several efficiencies such as acceptance of the PHOS detector, reconstruction efficiency and PID cuts efficiency. How to calculate them is described in this section.

3.6.1 Efficiency calculation

I used M.C. data containing HIJING which reproduce Pb-Pb collisions and added π^0 signal to reach at high p_{T}. These efficiencies can be simply combined and defined as Eq.14 in this analysis.

$$\text{acceptance} \times \text{efficiency} = \frac{\mathrm{N}_{\pi^0}^{\text{reconstructed}} \text{ after PID cuts}}{\mathrm{N}_{\pi^0}^{\text{generated}} \text{ in } |\mathrm{y}| < 0.5} \tag{14}$$

where $\mathrm{N}_{\pi^0}^{\text{reconstructed}}$ is the number of π^0 reconstructed in PHOS, $\mathrm{N}_{\pi^0}^{\text{generated}}$ is the number of π^0 generated in HIJING and single π^0 simulation.

3.6.2 Feed-down correction

π^0s decayed from other hadrons, mainly from K_s^0, must be considered. This decay feeds π^0 yields, so, this correction factor is called "feed-down efficiency".

$$\text{feed-down} = \frac{\mathrm{N}_{\pi^0}^{\text{generated with R < 1cm}}}{\mathrm{N}_{\pi^0}^{\text{generated}} \text{ in } |\mathrm{y}| < 0.5} \tag{15}$$

where, R is the distance between the collision point and the point where π^0 is generated. Since K_s^0 has long life time $c\tau \sim 2.7$cm, we can remove the contribution from this decay.

4 Results

In this section, results of my analyses and comparison to previous researches are described.

4.1 Raw yield

The raw yield of π^0simply shows how many π^0s I could measure with the PHOS detector. I measured π^0 yield in four centrality classes, 0-10%, 10-30%, 30-50% and 50-90%. Especially, I could measure π^0 in p_{T} range from 1 GeV/c to 35 GeV/c in the most central collisions as shown by red points on Figure.28.

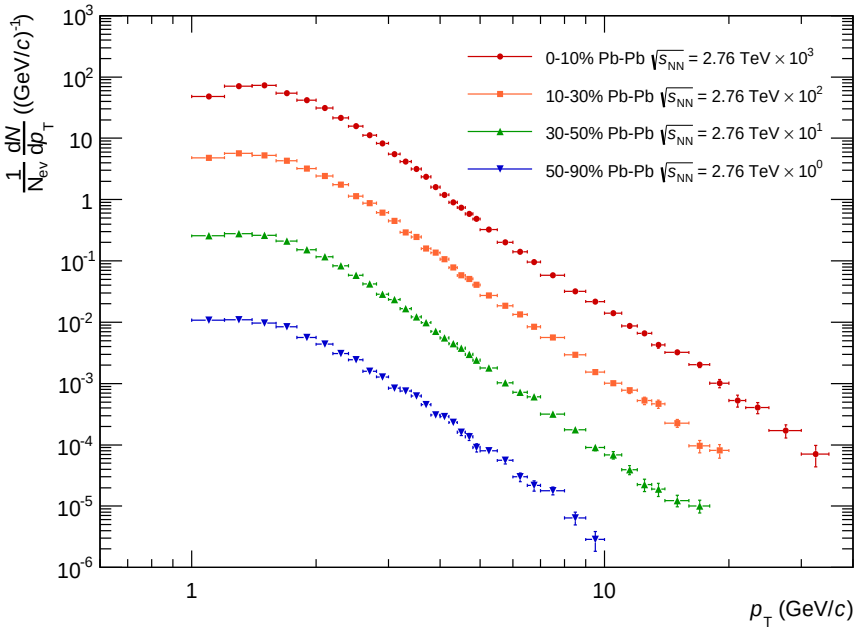

Figure 28: Raw yield of π^0. The red shows 0-10%, orange shows 10-30%, green shows 30-50% and blue shows 50-90%. Red, orange and green points are scaled to show these spectra clear.

The raw yield is not physics value because the raw yield depends on detector acceptance, PID cuts and so on. So, We need to measure the invariant yield by correcting raw yield with several efficiencies described in 3.6. The invariant yield is defined as Eq.18.

4.2 Efficiencies in M.C. analysis

The efficiency was calculated based on Eq.14 in 3.6. The p_{T}-dependent efficiency is shown on Figure.29.
Efficiency is degrading over 26 GeV/c in Figure.29. This is because in the rest frame of a parent particle π^0, when two photons decay to a perpendicular direction to Lorentz boost, the opening angle between two photons will be the smallest and two clusters will merge on this PHOS detector.

$$\tan\theta_{\mathrm{min}} = \frac{m}{p} \tag{16}$$

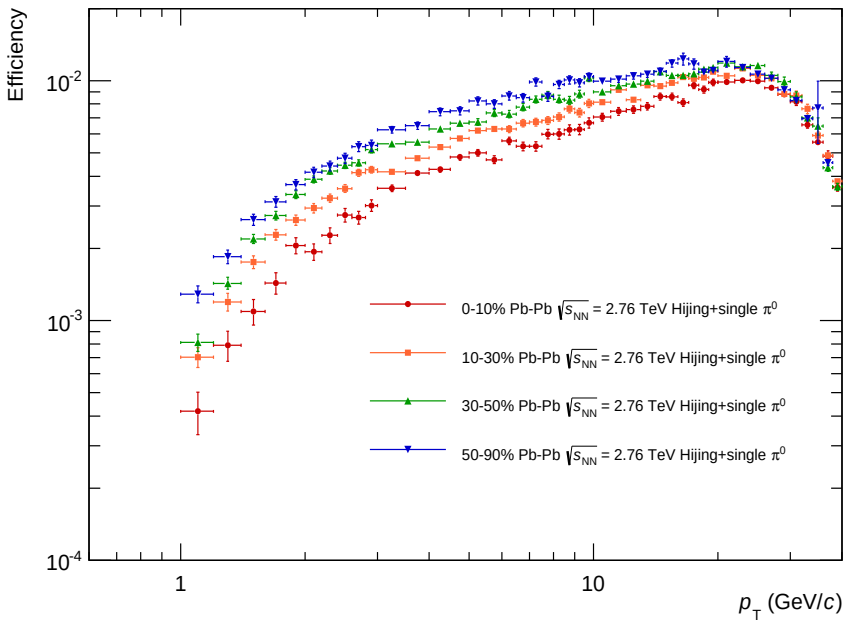

Figure 29: Efficiencies for π^0. The acceptance of the PHOS detector, reconstruction efficiency, PID-cut efficiencies such as common cluster cuts, CPV, dispersion cut and feed-down are included.

This merging effect will start when the distance between two clusters gets closer than 2.2 cm which is the size of a $PbWO_4$ crystal. The PHOS detector locates at 4.6 m from the interaction point. Therefore, a threshold of momentum of the parent particle can be calculated.

$$p_{\text{threshold}} = \frac{0.135}{\tan^{-1}\left(\frac{2.2}{460}\right)} = 28 \text{ GeV} \tag{17}$$

Monte-Carlo result is consistent with this calculation. However, this depends on clustering algorithm and can be improved in the future.

4.3 Invariant yield

The invariant yield is defined by Eq.18 and shown by Figure.30 in this analysis. We can not measure the production cross section ($\text{Pb} + \text{Pb} \rightarrow \pi^0 + \text{X}$) because there are several effects to increase and decrease yields in heavy-ion collisions. So, I will compare this invariant yield with that in pp collisions to study how much yields increase or decrease in Pb-Pb collisions.

$$E\frac{\mathrm{d}^3N}{\mathrm{d}p^3} = \frac{1}{2\pi \mathrm{N_{ev}}}\frac{\mathrm{d}^2N}{p_{\mathrm{T}}\mathrm{d}p_{\mathrm{T}}\mathrm{d}y} \tag{18}$$

However, we can measure the production cross section of π^0 ($\text{p} + \text{p} \rightarrow \pi^0 + \text{X}$) in pp collisions, defined as Eq.19. This cross section is an important reference to study a nuclear

modification factor $R_{\rm AA}$.

$$E\frac{{\rm d}^3\sigma}{{\rm d}p^3} = \frac{\sigma_{\rm pp}^{\rm inel}}{2\pi {\rm N_{ev}}}\frac{{\rm d}^2N}{p_{\rm T}{\rm d}p_{\rm T}{\rm d}y} = \sigma_{\rm pp}^{\rm inel}\times E\frac{{\rm d}^3N}{{\rm d}p^3} \tag{19}$$

To calculate $R_{\rm AA}$, the invariant yield in pp collisions at $\sqrt{s}$ = 2.76 TeV was fitted by Tsallis function[19] that can describe π^0 spectrum well, shown by Eq.20.

$$E\frac{{\rm d}^3N}{{\rm d}p^3} = \frac{A}{2\pi}\frac{(n-1)(n-2)}{nC[nC+m(n-2)]}\frac{1}{c^2}\cdot\left(1+\frac{\sqrt{m^2+p_{\rm T}^2}-m}{nC}\right)^{-n} \tag{20}$$

where c is the speed of light, m is the mass of π^0 (0.135 GeV/c^2). Parameterization from [1] is summarized in Table.5. $R_{\rm AA}$ should be calculated with data points in each pp and Pb-Pb collisions. However, bin-width of my histograms is different from that of published pp results. Therefore, $R_{\rm AA}$is calculated based on Tsallis function parameterized on Table.5 given by [1].

Table 5: Parameterization of Tsallis function for $R_{\rm AA}$.[1]

system	A	C (MeV/c^2)	n
pp at $\sqrt{s}$ = 2.76 TeV	17 ± 0.7	135 ± 29	7.1 ± 0.7

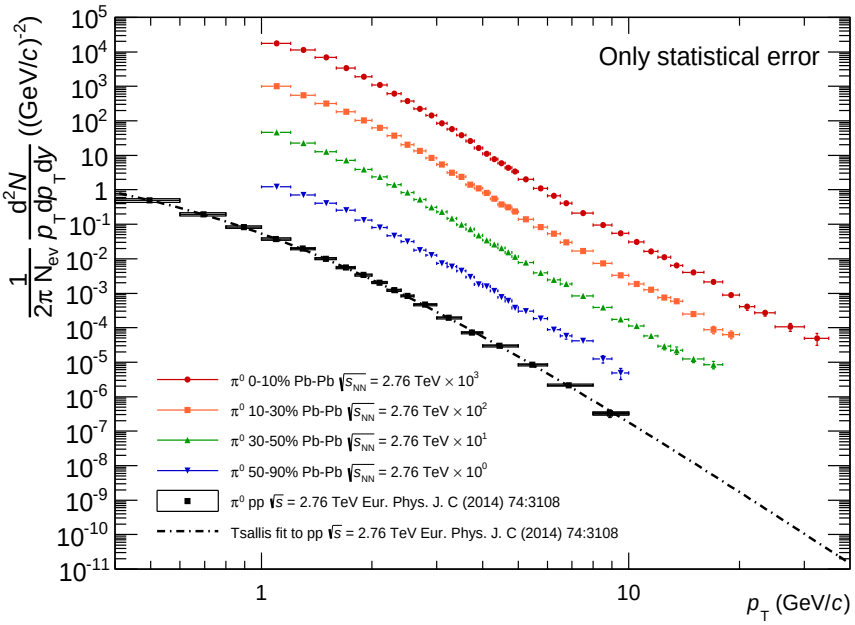

Figure 30: π^0 invariant yield

4.4 Nuclear modification factor $R_{\rm AA}$

The nuclear modification factor $R_{\rm AA}$ is defined by Eq.3. The $R_{\rm AA}$ shows how much yields of the hadron are modified in Pb-Pb collisions. If the QGP is created in the Pb-Pb

collision, $R_{\rm AA}$ will be less than unity. Results in my analysis are shown on Figure.31. $T_{\rm AA}$ is a nuclear overlap function, which means effective luminosity of nucleon in the collision processes. It relates to the average number of inelastic nucleon-nucleon collisions as Eq.21.

$$T_{\rm AA} = \frac{N_{\rm coll}}{\sigma_{\rm pp}^{\rm inel}} \tag{21}$$

where $N_{\rm coll}$ is the number of binary collisions, $\sigma_{\rm pp}^{\rm inel}$ is an inelastic cross section in pp collisions and $\sigma_{\rm pp}^{\rm inel} = 62.8^{+2.4}_{-4.0} \pm 1.2$ mb at $\sqrt{s} = 2.76$ TeV [18].

Table 6: $T_{\rm AA}$value used in this analysis.[5]

centrality	0-10%	10-30%	30-50%	50-90%
$T_{\rm AA}({\rm mb}^{-1})$	23.88	11.79	3.932	0.5698

$R_{\rm AA}$ is less than unity in all centrality classes for $p_{\rm T} > 3{\rm GeV}/c$. The level of suppression is the strongest in the most central collisions 0-10%, and increases with centrality from about 0.12 at 0-10% to 0.6-0.8 in 50-90%. With regards to $p_{\rm T}$ dependence, $R_{\rm AA}$ has the maximum value around $p_{\rm T}$=1-2 GeV/c, decreases to 4 GeV/c, almost constant value from 4 GeV/c to 10 GeV/c, gradually increases from 10 GeV/c.

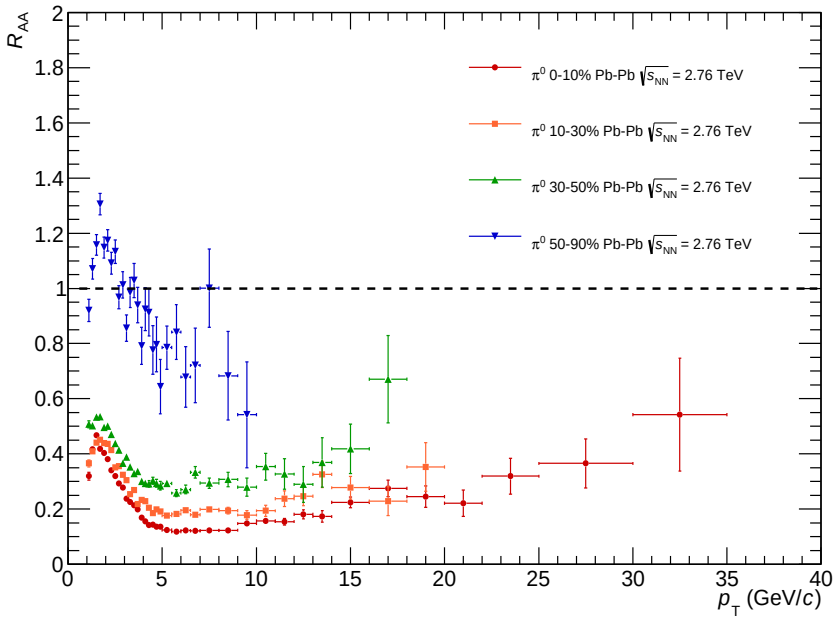

Figure 31: $R_{\rm AA}$ of my analysis as a function of $p_{\rm T}$. Red shows $R_{\rm AA}$ in 0-10%, orange:10-30%, green:30-50%, blue:50-90% respectively. The strong suppression is observed in the most central collisions. It reaches down to 0.12 at $p_{\rm T}$=5.5GeV/c. in 0-10%

5 Discussion

5.1 Comparison to 2010 data

Pb-Pb data were taken in also 2010. The comparison of results between using data taken in 2010 and 2011 is required to check validity of my analysis. Therefore, I compared my results, namely, the invariant yield and R_{AA} of π^0 with those published in 2014. I measured π^0 in four centrality classes (0-10, 10-30, 30-50, 50-90%) to avoid drops in centrality distribution as shown by Figure.20, but centrality class is separated to six (0-5, 5-10, 10-20, 20-40, 40-60, 60-80%) in published data[1]. Centrality classes are different, so, results in only the most central collision 0-10% were described.

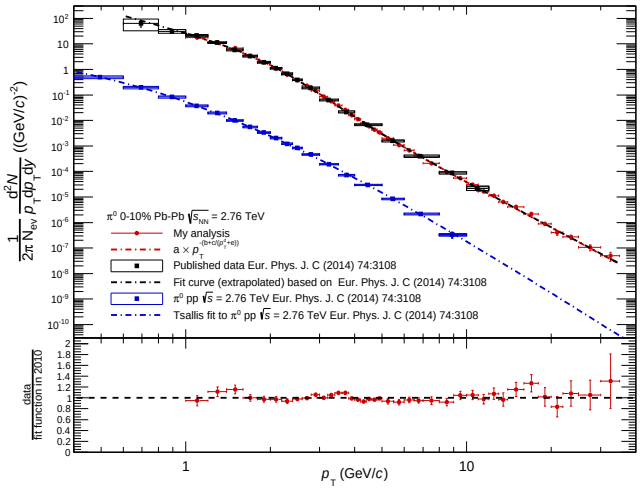

(a) Invariant yield

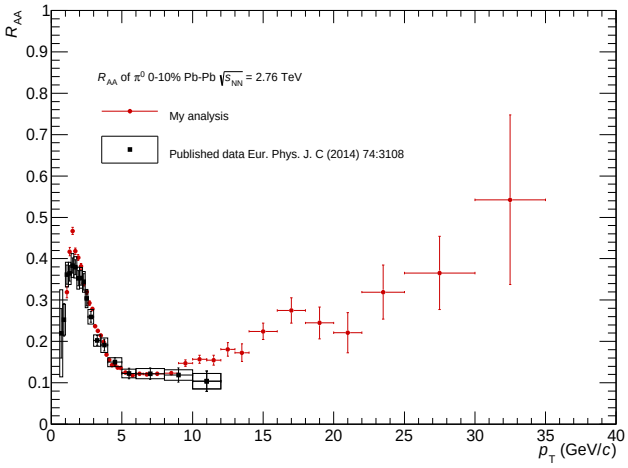

(b) R_{AA}

Figure 32: Comparison to 2010 data[1].

The invariant yield in published data[1] was fitted with a function 22 [1]. My result was also fitted with this function as shown by Figure.32a top, and divided by the fitting function parameterized by 2010 result on Figure.32a bottom. Finally, R_{AA} is also consistent in p_{T}

< 10 GeV/c region.

$$\frac{1}{2\pi \mathrm{N_{ev}}} \frac{\mathrm{d}^2 N}{p_{\mathrm{T}} \mathrm{d}p_{\mathrm{T}} \mathrm{d}y} = a \times p_{\mathrm{T}}^{-(b+c/(p_{\mathrm{T}}^{d}+e))} \tag{22}$$

Table 7: Parameterization of fitting function 22.

Parameter	a $(\mathrm{GeV}/c)^{-2}$	b	c	d	e
Published [1]	25.53	5.84	-49.95	3.35	18.49

According to this comparison of the invariant yield, it is proved that my analysis is consistent with published data. Additionally, my result reaches up to 35 GeV/c in p_{T} range, which is the first measurement of π^0 at high p_{T} due to much statistics than data in 2010.

5.2 Comparison of $R_{\rm AA}$ between π^0 and $\pi^{\pm}$, $K^{\pm}$

The nuclear modification factor $R_{\rm AA}$ of charged particles at large transverse momenta in both pp and Pb-Pb collisions at $\sqrt{s_{\rm NN}} = 2.76$ TeV has been measured in the ALICE[20]. I compared $R_{\rm AA}$ of π^0 with that of $\pi^{\pm}$, $K^{\pm}$.

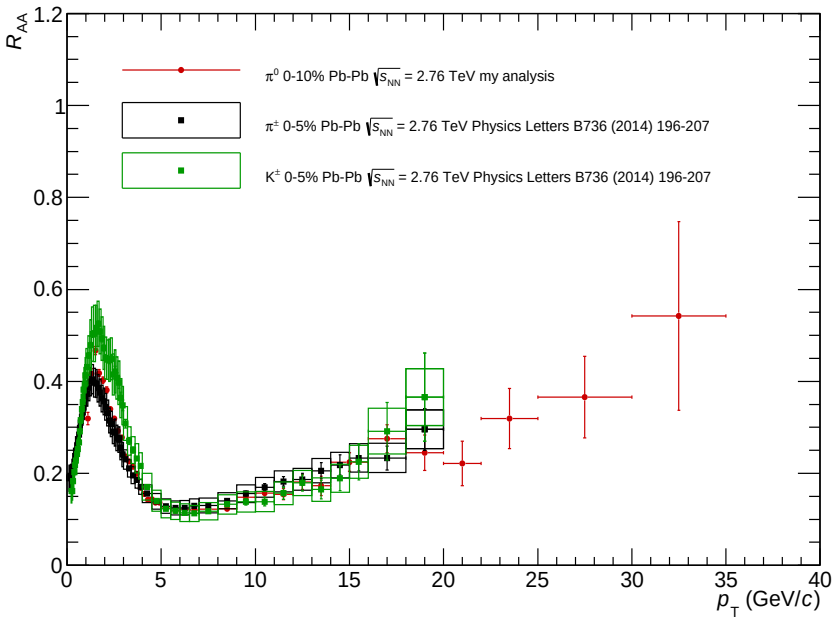

Figure 33: $R_{\rm AA}$ of π^0, $\pi^{\pm}$ and $K^{\pm}$ [20].

$R_{\rm AA}$ of π^0 and $\pi^{\pm}$ are consistent with each other in all measured p_{T} region. On the other hand, $K^{\pm}$s are suppressed less than neutral and charged pions in $p_{\mathrm{T}} < 4$GeV/c. This result indicates the energy-loss which modifies yields of hadrons strongly relates mass ordering. For $p_{\mathrm{T}} > 4$GeV/c, $R_{\rm AA}$ of all pions and charged kaons are consistent with each other at least up to 20 GeV/c.

6 Conclusion

Invariant yields of π^0 in $|y| < 0.5$ is measured in Pb-Pb collisions at $\sqrt{s_{\rm NN}} = 2.76$ TeV with the PHOS detector in four centrality classes (0-10, 10-30, 30-50, 50-90%) from 1 GeV/c to 35 GeV/c in a $p_{\rm T}$ range. The maximum $p_{\rm T}$ reaches up to 35 GeV/c in the most central collisions 0-10%. This is the first measurement of π^0 at such high $p_{\rm T}$ region of all heavy-ion collider experiments. The nuclear modification factor $R_{\rm AA}$ indicates strong suppression of π^0 in the most central collisions by a factor of 10 around $p_{\rm T} = 6$ GeV/c. Finally, the comparison of $R_{\rm AA}$ between π^0, $\pi^{\pm}$ and $K^{\pm}$ has been performed. $R_{\rm AA}$of π^0 and $\pi^{\pm}$ are consistent with each other in all measured $p_{\rm T}$ region. On the other hand, $R_{\rm AA}$of pions and charged kaons are different below $p_{\rm T} = 4$ GeV/c. This result exhibits energy-loss at parton level and mass ordering. However, only statistical error is taken into account. I have to estimate systematic uncertainties. I hope these results will be combined with other subsystems (EMCAL, PCM) and compared to theoretical models later to study energy-loss more precisely.

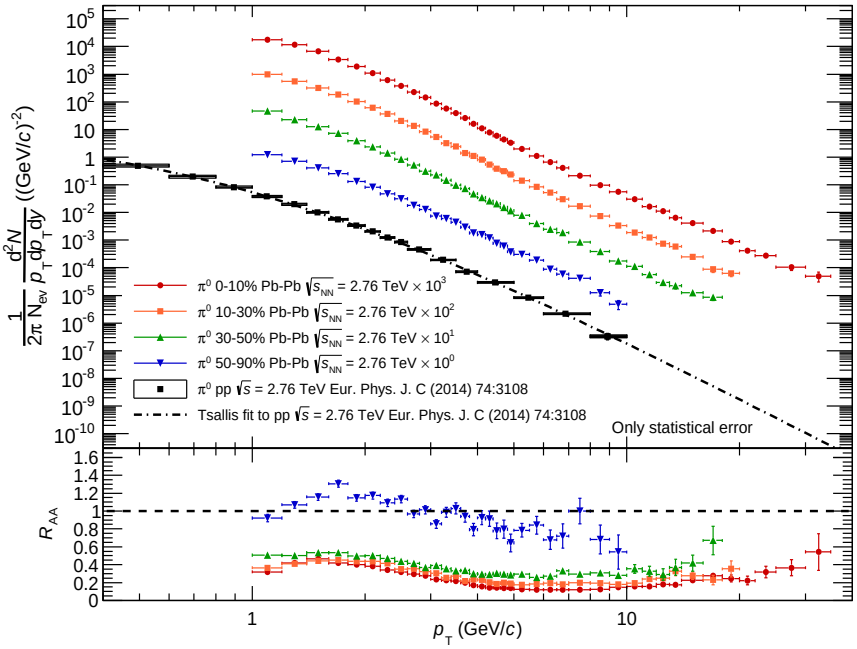

Figure 34: Invariant yields and $R_{\rm AA}$ of π^0 with the PHOS detector using 2011 data.

Acknowledgement

First of all, I would like to thank Professor Toru Sugitate for assisting by his grant-in-aid. He also told me general strategy to fight and to construct the PHOS detector in a large experiment. I acknowledge all stuffs in Hiroshima University, Professor Kenta Shigaki, Dr. Kensuke Homma and Dr. Takahiro Miyoshi. All staffs gave me many important comments at the meeting. I would like to thank Dr. Yuri Kharlov (Institute for High Energy Physics (RU)) and Dr. Dmitri Pressunko (National Research Centre Kurchatov Institute (RU)) who are conveners in a PHOS analysis group. They helped me to do this analysis from the beginning. Especially, Dr. Yuri Kharlov helped me when I stayed at CERN to commission the PHOS detector for Run-2 during the LS1. I would like to thank all PHOS collaborators for constructing and operating the PHOS detector. In addition, I would like to thank ALICE-Japan members. They supported my CERN life. Daisuke Watanabe who is a senior colleague in Tsukuba taught me how to operate SRUs, Front-End Electronics cards and how to solve technical problems kindly. Not only hardware problem, he demonstrated how to install and use ALICE offline-analysis framework for me. I could not start this analysis without his instruction. I acknowledge senior colleagues in Hiroshima University, Satoshi-san ,Okubo-san, and Hasebe-san. Finally, I would like to thank my colleagues, Nagashima-kun, Tanizaki-san, Yuasa-kun and Nakazato-kun. They always helped me kindly. Thank you, everyone.

Daiki Sekihata 10.February.2015

References

[1] B.Abelev *et al.*, ALICE Collaboration, Eur. Phys. J. C (2014) 74-3108

[2] F. Karsch Lect.Notes Phys. 583 (2002) 209-249

[3] GSI official web site https://www.gsi.de/

[4] ALICE Japan official web site http://alice-j.org/

[5] B.Abelev *et al.*, ALICE Collaboration, PHYSICAL REVIEW C 88, 044909 (2013)

[6] KOHSUKE YAGI, TETSUO HATSUDA AND YASUO MIAKE, Quark-Gluon Plasma, CAMBRIDGE MONOGRAPHS ON PARTICLE PHYSICS, NUCLEAR PHYSICS AND COSMLOGY

[7] PHENIX official web site http://www.phenix.bnl.gov/

[8] M.M.Aggarwal *et al.*, WA98 Collaboration, Phys.Rev.Lett.85.3595 (2000)

[9] Lyndon Evans and Philip Bryant 2008 JINST 3 S08001

[10] The ALICE Collaboration *et al* 2008 JINST 3 S08002

[11] The ATLAS Collaboration *et al* 2008 JINST 3 S08003

[12] The CMS Collaboration *et al* 2008 JINST 3 S08004

[13] The LHCb Collaboration *et al* 2008 JINST 3 S08005

[14] B.Abelev *et al.*, ALICE Collaboration, Int. J. Mod. Phys. A 29 (2014) 1430044

[15] ALICE collaboration, Technical design report of the electromagnetic calotimeter, CERN-LHCC-2008-014

[16] D.V. Aleksandrov *et al.* Nuclear Instruments and Methods in Physics Research A 550 (2005) 169184

[17] ALICE collaboration, Technical design report of the photon spectrometer, CERN-LHCC-99-004

[18] B.Abelev *et al.*, ALICE Collaboration, Eur. Phys. J. C (2013) 73:2456

[19] Constantino Tsallis, Journal of Statistical Physics, Vol. 52, Nos. 1/2, 1988

[20] B.Abelev *et al.*, ALICE Collaboration, Physics Letters B736 (2014) 196207